A Continuum Meshfree Method for Sandbox-style Numerical Modeling of Accretionary and Doubly Vergent Wedges

Enrique M. del Castillo[a], Alomir H. Fávero Neto[b] and Ronaldo I. Borja[a,*]

[a]*Department of Civil and Environmental Engineering, Stanford University, 473 Via Ortega, Stanford, CA 94305, USA*
[b]*Department of Civil and Environmental Engineering, Bucknell University, 1 Dent Drive, Lewisburg, PA 17837, USA*

ARTICLE INFO

Keywords:
Accretionary wedges
Doubly vergent orogens
Meshfree continuum method
Geodynamical modeling
Smoothed particle hydrodynamics
Critical taper theory

ABSTRACT

In this study we introduce and utilize `GEOSPH`, a Lagrangian particle-based continuum Smoothed Particle Hydrodynamics (SPH) code to simulate the deformation of geologic materials in sandbox-style experiments using an elastoplastic constitutive model. Due to the meshfree nature of SPH, our proposed framework is capable of handling the large deformations characteristic of sandbox-style experiments. SPH is also able to capture strain localization and discontinuities, allowing us to resolve faulting patterns emerging in the sandbox experiments. We successfully validate our SPH implementation against the benchmark experiments of Buiter and co-workers, and then apply SPH to understand the deformational processes occurring in doubly vergent orogens resultant from the S-point experimental setup and from finitely high wedge-like indenter backstops of different inclinations. We find that the topographic slope of the prowedge results from the competing processes of vertical uplift due to the indenter and forward thrusting, while the topographic slope of the retrowedge is a product of repeated shallow slope failure. Our findings show that SPH is a promising numerical method which should be added to the current palette of computational tools used by structural geologists for solving problems relating to tectonics and crustal deformation.

1. Introduction

Sandbox-style experiments have enabled the simulation of faulting, the formation of orogenic wedges, rifting, and other geodynamical phenomena occurring in the Earth's crust (Buiter et al., 2006, 2016; Wolf et al., 2003; Herbert et al., 2015), and analogue sandbox experiments using sand or other frictional materials have been used to study tectonic phenomena since at least the 19th century (Graveleau et al., 2012). However, while it is easy to draw conclusions on the geometry and structural styles recreated in analogue sandbox experiments, it is difficult to determine the state of stress within the experiment, to accurately observe strain localization patterns, to freeze time and gravity, or to backtrack and re-initiate the simulation from a previous state. Numerical modeling used to solve the initial boundary value problems (IBVP) describing the mechanics of the

---

*Corresponding author. Tel.: +1 (650) 723-3664
Email addresses: `emdc@stanford.edu` (E.M. del Castillo); `ahf009@bucknell.edu` (A.H. Fávero Neto); `borja@stanford.edu` (R.I. Borja)
ORCID(s): `0000-0002-7505-1705` (E.M. del Castillo); `0000-0002-1202-2958` (A.H. Fávero Neto)

sandbox, can help tackle the geological questions analogue sand-boxes were designed to address, while overcoming their shortcomings (Gray et al., 2014; Buiter et al., 2006).

Mesh-based continuum methods such as the Finite Element Method (FEM) are perhaps the most important and best known numerical approach used to solve the IBVPs governing geological and geodynamical processes (Borja and Dreiss, 1989; Borja and Aydin, 2004; Crook et al., 2006; Sanz et al., 2008), but have difficulty simulating the large deformations observed in sandbox-style experiments due to severe mesh entanglement and distortion. While work-arounds exist such as Arbitrary Lagrangian Eulerian (ALE) FEM, which require re-meshing, they come with a certain computational and accuracy penalty (Hu and Randolph, 1998). Mesh-based methods without enhancements also have difficulty when dealing with processes involving discontinuities such as faulting, requiring fault paths to be predetermined (Sanz et al., 2007; Gray et al., 2014), unless enhancements such as strong discontinuities (Simo et al., 1993; Borja, 2000; Borja and Regueiro, 2001; Liu, 2020; Jameei and Pietruszczak, 2020), phase field (Shiozawa et al., 2019; Zhou and Xia, 2019; Zhou and Zhuang, 2020; Yang et al., 2021), or extended finite elements (Belytschko and Black, 1999; Liu and Borja, 2008, 2013; Liu et al., 2019; Feng and Gray, 2019) are introduced. For capturing strain localization, a “seed,” or a material heterogeneity, is usually introduced in the model to induce strain localization in the first place, rather than occurring naturally (Kaus, 2010; Borja et al., 2013a,b; Song and Borja, 2014a,b).

Due to the disadvantages of mesh-based methods, certain meshfree methods such as the Discrete Element Method (DEM), which do not rely on element connectivity, are a popular alternative (Morgan and Boettcher, 1999; Burbidge and Braun, 2001; Naylor and Sinclair, 2005; Egholm et al., 2007; Gardner and Sitar, 2019; Ma et al., 2019; Zhao and Liu, 2020). However, DEM is computationally expensive, severely limiting the scale of experiments. Furthermore, if linkage back to the continuum scale is desired to discern stress or strain fields from the distinct particles, an averaging process of inter-granular forces or displacements must be performed, involving additional calculation (Yan and Regueiro, 2019; Shen et al., 2019; Nguyen et al., 2020; Jiang et al., 2020; Wu et al., 2020). Alternative methods to both FEM and DEM include a class of continuum particle methods such as the material point method (Chandra et al., 2021; Kularathna et al., 2021), peridynamics (Sun and Fish, 2021; Song and Menon, 2019), particle finite element method (Yuan et al., 2021; Wang et al., 2021; Jin et al., 2020), and smoothed particle hydrodynamics, or SPH (Sheikh et al., 2020; Zhan et al., 2020). Originally developed for astrophysical problems (Gingold and Monaghan, 1977; Lucy, 1977), the SPH method has a number of desirable features that make it suitable for the problem addressed in this paper.

SPH is a meshfree, continuum-based, Lagrangian method, where particles represent pieces of a continuum body and thus possess continuum level field variables and properties (i.e., mass, density, velocity, etc). The values of these fields for each particle are determined by an interpolation from neighboring particles using a weighted sum and a kernel function. The meshfree nature of SPH allows it to handle large deformation problems like in DEM, while having improved scalability over DEM (Peng et al., 2019; Nguyen et al., 2020; Tran et al., 2019; Longo et al., 2019; Xu et al., 2020a,b). Strain localization and kinematic discontinuities characteristic of faulting have also been shown to arise naturally in SPH (del Castillo et al., 2021; Fávero Neto and Borja, 2018; Fávero Neto et al., 2020; Wang et al., 2020; Su et al., 2021). As explained in del Castillo et al. (2021), strain localization in the form of shear bands can be roughly considered analogous to faults in the context of SPH. For this reason, throughout the paper, the terms shear band, fault, or thrust are used interchangeably.

In this paper, we apply `GEOSPH` (del Castillo et al., 2021; Fávero Neto, 2020), a parallel SPH code built on the on the open-source Python-based framework `PySPH` (Ramachandran et al., 2020), designed to handle the deformation of geologic materials across scales, for sandbox-style modeling of accretionary wedges, and doubly vergent orogenic wedges. Deformation of rock in orogens and accretionary wedges at the field scale and of sand at the sandbox scale, is characterized by elastic and plastic behavior, large deformations, strain localization, and faulting, which is well described by non-associative, pressure sensitive elastoplastic constitutive models and the Mohr-Coulomb or Drucker-Prager yield criteria (Jaeger and Cook, 1979; Panian and Wiltschko, 2007; Gray et al., 2014). We use the Drucker-Prager yield criterion, which is a two invariant smooth approximation of the Mohr-Coulomb yield surface. The Drucker-Prager approximation plots as a circle in the deviatoric plane, while the Mohr-Coulomb yield surface is hexagonal, and thus is easier to implement and has improved numerical stability especially for three-dimensional problems. The Drucker-Prager criterion has been successfully employed in a number of other tectonics modeling studies (Niño et al., 1998; Cardozo et al., 2003; Panian and Wiltschko, 2007; Stockmal et al., 2007).

While using elastoplasticity for modeling tectonic deformation has become increasingly more common in the geological and geodynamical modeling communities (Crook et al., 2006; Sanz et al., 2007, 2008; Nollet et al., 2012; Albertz and Sanz, 2012; Gray et al., 2014; Reber et al., 2020; Scovazzi et al., 2021) primarily at the reservoir or fault scale, or whenever high fidelity projections of stress or strain are needed, this approach is currently less prevalent than Stokes flow modeling. Initially gaining popularity for its successful application to modeling mantle convection (Fullsack, 1995; Gerya and Yuen, 2007), and also for its relatively simpler implementation, tectonic crust is treated as a nonlinear fluid governed by the Stokes flow equations, and is used especially on the basin as opposed to the reservoir scale (Simpson, 2006; Ruh et al., 2012; Buiter et al., 2016). The effects of plasticity are usually incorporated into the equations via a nonlinear viscosity term. The only effort to model tectonic deformation to date using SPH (the doctoral thesis of Schwaiger (Schwaiger, 2007)), followed this approach by discretizing and solving the Stokes flow equations, but encountered difficulties resolving strain localization, and the results only achieved rough qualitative agreement with other modeling attempts using, for example, DEM.

`GEOSPH` is able to reproduce the expected geometry and kinematics of other analogue and numerical sandbox experiments, while providing useful stress, strain, and strain rate data often absent from most non-continuum simulations. We show that modeling crust as an elastoplastic medium yields considerably improved results across all geological dimension scales compared with previous attempts solving the Stokes equations with SPH. In this paper, we first validate our SPH implementation against a number of benchmark experiments from Buiter et al. (2006) and Buiter et al. (2016), namely, the stable wedge experiment in Section 4.1, the accretionary wedge shortening experiment in Section 4.2, and the S-point experiment in Section 4.3. In addition to performing these benchmark experiments showcasing the potential of SPH towards modeling large deformation mechanical problems in the geological sciences, our results also provide new insights into the role the backstop geometry in forearc basins plays in dictating the structural styles and strain localization patterns that emerge in sandbox models of doubly vergent wedges. We begin with brief overviews of critical taper theory and different orogenic wedge types in Section 2, and then of the governing equations solved in our SPH implementation and of the SPH method itself in Section 3. For a full description of SPH and our proposed framework, the reader is referred to del Castillo et al. (2021) and Fávero Neto (2020).

2. Accretionary Wedges, Critical Taper Theory, and Doubly Vergent Wedges

In contractional tectonic settings, crustal material accretes as sequences of successive thrust sheets forming an overall wedge-shaped mountain belt or orogenic wedge (alternatively accretionary wedge or thrust wedge) above the décollement, the weak basal detachment. The formation of mountain belts and orogenic wedges is arguably one of the most widely studied and complex processes in structural geology, and orogenic wedges are also the setting for important hydrocarbon deposits, and megathrust earthquakes (Bilotti and Shaw, 2005; Pollard and Fletcher, 2005; Elliott et al., 2016). At a broad level, the dynamics of accretionary wedge growth and formation is well understood through the classic bulldozer analogy of Davis et al. (1983). As a bulldozer pushes up a snow covered ramp or driveway, snow begins to accumulate at the front of the bulldozer's plow, and a snow wedge will form in front of the plow, growing until a constant wedge "taper" is reached. At this point the wedge reaches the so-called state of "critical taper", and the wedge grows self-similarly with internal deformation such as faulting helping to maintain the taper (Davis et al., 1983).

To first order, the overall geometry or taper of wedges can be described by an elegant analytical solution, known as the critical taper model, formally presented in the work of Dahlen (1984). The wedge's taper is defined as the sum of the angles $\alpha + \beta$, where β is the basal angle, or the angle between the horizontal and the décollement or base, while α, or the topographic angle, is the angle between the horizontal and the top surface of the wedge. The critical taper equations describe the possible range of tapers orogenic wedges can take for the wedges to remain mechanically stable. In the solution, the wedges are assumed to be at the critical state where the wedge grows self-similarly, and the material inside the wedge is assumed to be entirely at the point of failure. In the critical taper solution, the wedge taper $\alpha + \beta$ is a function of the strength of the wedge and base, and also of the pore fluid ratios of the wedge and base. When the wedge is dry, or there is no pore fluid, the taper reduces to a function of wedge and basal strength, as seen in the following equations:

$$\alpha + \beta = \Psi_b - \Psi_0 \tag{1}$$

where

$$\Psi_b = \frac{1}{2}\arcsin\left(\frac{\sin\phi_b}{\sin\phi}\right) - \frac{1}{2}\phi_b \tag{2}$$

and

$$\Psi_0 = \frac{1}{2}\arcsin\left(\frac{\sin\alpha}{\sin\phi}\right) - \frac{1}{2}\alpha. \tag{3}$$

In Equations (1–3), Ψ_b is the angle between the maximum principal stress σ_1 and the base, and Ψ_0 is the orientation of σ_1 with respect to the wedge top. Parameters Ψ_b and Ψ_0 depend on ϕ and ϕ_b, which are the internal angle of friction of the wedge and the base, respectively, and Ψ_0 also depends implicitly on the topographic slope α (Dahlen, 1984). The critical taper solution is graphically displayed as a "flounder" or envelope diagram with two "branches" of tapers for a given ϕ and ϕ_b, where the wedge is on the verge of failure throughout, with tapers on the upper branch of the envelope in extensional failure, and tapers on the lower branch in compressional failure. Inside the envelope, wedges are stable and can slide along the décollement without internal deformation as long as no new material is accreted. In general, there has been good agreement between tapers observed in the field and those measured from analogue and numerical experiments, with those predicted by the critical taper solution (Davis et al., 1983). Nevertheless, the critical taper model provides little insight into the internal deformation of the wedge, and also fails to account for the more complicated deformation processes arising in continental collisions or forearcs as pointed out by Koons (1990). In the critical taper model, the backstop (also indenter), or crust, of higher rigidity compressing the accreting sediment or rock (i.e. the bulldozer) is assumed to be of considerably greater height than the material being accreted. However, this is rarely the case, and usually mass flow over the backstop occurs, resulting in a two-sided wedge or doubly vergent wedge.

Significant progress has been made over the last few decades concerning the mechanics of doubly vergent wedges thanks to a combination of analogue and numerical sandbox-style experimental studies (Byrne et al., 1993; Willett et al., 1993; Beaumont et al., 1996; Wang and Davis, 1996; Willett, 1999; Bonini et al., 1999; Persson, 2001; Naylor and Sinclair, 2005; Simpson, 2011). However, unanswered questions remain regarding the applicability of the critical taper model to the distinct parts of the doubly vergent wedge, namely, the prowedge (forward facing towards the direction of shortening) or retrowedge (backwards facing) (Buiter et al., 2016).

3. Numerical Implementation

The SPH method solves the conservation of mass and momentum equations (Equations 4 and 5, respectively), which are the governing equations of the purely mechanical initial boundary value problem over domain Ω and time t:

$$\dot{\rho} + \rho \nabla \cdot \boldsymbol{v} = 0 \quad \forall \boldsymbol{x} \text{ in } \Omega \times t \tag{4}$$

$$\nabla \cdot \boldsymbol{\sigma} + \boldsymbol{b} = \rho \dot{\boldsymbol{v}} \quad \forall \boldsymbol{x} \text{ in } \Omega \times t \tag{5}$$

where $\dot{\rho}$ is the material time derivative of the density field, $\dot{\boldsymbol{v}}$ is the material time derivative of the velocity field, $\boldsymbol{b}$ is a body force vector, and $\boldsymbol{\sigma}$ is the Cauchy stress tensor.

In the SPH method, the continuous problem domain is discretized into a series of particles which possess continuum level properties such as mass, density, velocity, etc. The value of each material property, denoted $f(\boldsymbol{x})$, is found for a particular particle using the following convolution integral over the domain Ω:

$$\langle f(\boldsymbol{x}) \rangle = \int_{\Omega} f(\boldsymbol{x}') W(\boldsymbol{x} - \boldsymbol{x}', h) \mathrm{d}\boldsymbol{x}'. \tag{6}$$

Here, W is the kernel (or smoothing function), which serves as a weighting function, and h is the smoothing length, which controls the size of the integration domain Ω. The smoothing length serves as a numerical characteristic length scale leading to non-local properties in SPH. Ensuring that the smoothing length is maintained fixed as the discretization refinement changes, removes any discretization dependance of the solution, which is a significant advantage of the SPH method, and renders non-local constitutive models which might otherwise be employed to regularize the solution, redundant (Vignjevic et al., 2014).

The continuous integral for the material property $f(\boldsymbol{x})$ for a particle i at position $\boldsymbol{x}$ can be approximated by the summation

$$\langle f(\boldsymbol{x}) \rangle_i \approx \sum_{j=1}^{N} \frac{m_j}{\rho_j} f(\boldsymbol{x}_j) W(\boldsymbol{x} - \boldsymbol{x}_j, h) \tag{7}$$

over all particles j in the support domain of i. Likewise, $\partial f(\boldsymbol{x})/\partial \boldsymbol{x}$ can be approximated by

$$\left\langle \frac{\partial f(\boldsymbol{x})}{\partial \boldsymbol{x}} \right\rangle_i \approx \sum_{j=1}^{N} \frac{m_j}{\rho_j} f(\boldsymbol{x}_j) \left[\frac{\partial W(\boldsymbol{x} - \boldsymbol{x}_j, h)}{\partial \boldsymbol{x}} \right]_i . \tag{8}$$

Using the approximations of generic material properties $f(\boldsymbol{x})$ and of their derivatives $\partial f(\boldsymbol{x})/\partial \boldsymbol{x}$, the governing equations (Equations 4 and 5) can be deconstructed and similarly approximated.

In our SPH formulation, the geomaterial is modeled as an elastic-perfectly plastic material with a non-associative flow rule on the Drucker-Prager yield criterion. In this model, the material deforms elastically until its state of stress satisfies the yield criterion, and henceforth the material deforms plastically. To determine the appropriate deformation regime for the elastoplastic material, the Drucker-Prager criterion is introduced, and is given by

$$\mathcal{F}(I_1, J_2) = \sqrt{2J_2} + \alpha_\phi I_1 - k_c \leq 0 \tag{9}$$

where $J_2 = \|\boldsymbol{s}\|^2/2$ is the second invariant of the deviatoric stress tensor, $\boldsymbol{s}$, and $I_1 = \mathrm{tr}[\boldsymbol{\sigma}]$ is the first invariant of the Cauchy stress tensor. The parameters α_ϕ and k_c are the Drucker-Prager parameters, which can be related back to the Mohr-Coulomb parameters, namely, the angle of internal friction ϕ and the cohesion c of the material, respectively. For expressions of α_ϕ and k_c as functions of the Mohr-Coulomb parameters, see Borja (2013).

In sandbox-style experiments, walls or solid boundaries usually delimit the analogue or computational particles and multiple approaches exist for handling these types of boundary conditions in SPH (Liu and Liu, 2003; Violeau, 2012; Fávero Neto, 2020). In our SPH code, the dynamic boundary condition formulation of Adami et al. (2012) is used. The solid boundaries are discretized into layers of so-called boundary particles, which are fixed or move at a prescribed velocity, and help avoid penetration of the boundaries by the domain particles. However, the formulation of Adami et al. (2012) is not a perfect Coulomb boundary condition, and we are also not able to control the effective friction angle at the boundary interface ϕ_b. Another limitation of these boundary conditions specific to sandbox experiments, is that it is not possible to prevent slippage from occurring along the boundary-sand interface, which is generally not desired along the backstop. For these reasons, and given the importance of the basal friction angle along the décollement in orogenic wedges and critical taper theory, it is important to determine the effective basal friction angle in our simulations.

For this purpose, we performed a series of numerical experiments of infinite slopes where the solid boundary at the bottom of the slope is modeled using Adami et al. (2012)'s formulation and periodic boundary conditions are used in the x-direction (the slope plane). Two slope models with inclinations $\alpha = 30°$ and $60°$ were created, and the Mohr-Coulomb internal friction angle parameter ϕ was varied from $\phi = 20°$ to $50°$ for each slope inclination. In all of our simulations in this paper, a very small rate of loading (and strain) is used, so we have quasi-static conditions (see Section 4). Hence, the static basal friction angle ϕ_b is determined at each value of ϕ in the two slope models.

To find the static basal friction angle, the average state of stress $\overline{\boldsymbol{\sigma}}$ in the layers adjacent to the bottom boundary was determined, and the Coulomb friction angle was calculated as

$$\phi_b = \arctan\left(\frac{N}{T}\right) \tag{10}$$

where N and T are, respectively, the normal and shear components of traction on the boundary surface, given as

$$N = \overline{\boldsymbol{\sigma}} : \ (\boldsymbol{n} \otimes \boldsymbol{n}) \tag{11}$$

$$T = \overline{\boldsymbol{\sigma}} : \ \left(\boldsymbol{n} \otimes \boldsymbol{n}_t\right). \tag{12}$$

In the previous equations, $\boldsymbol{n}$ and $\boldsymbol{n}_t$ are the unit normal and unit tangential vectors to the boundary surface, respectively. Using linear regressions of the measured ϕ_b with respect to ϕ in the $\alpha = 30°$ and 60° infinite slopes, a relation between the static basal friction and the internal angle of friction was determined to be:

$$\phi_b = 0.79\phi. \tag{13}$$

Figure 1 shows the variation of the basal friction angle versus the internal friction angle of the material simulated, as well as the computed linear regressions used to find Equation 13. We use Equation 13 to calculate the expected basal friction ϕ_b given a particular ϕ, which we assign to the soil or wedge particles in our subsequent simulations.

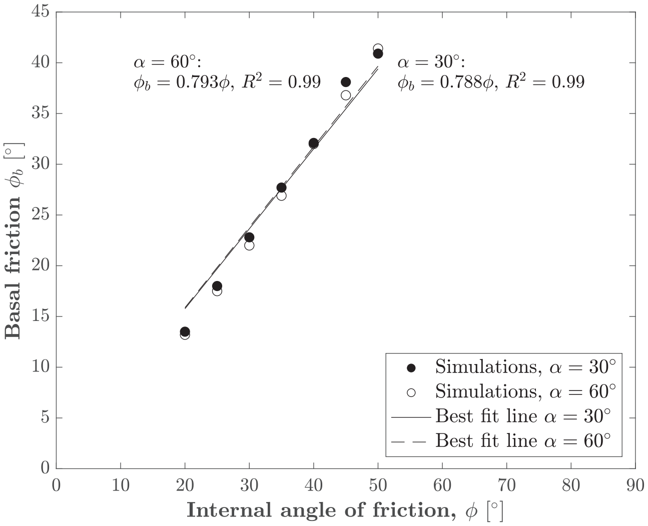

Figure 1: Variation of basal friction angle with internal friction angle for Adami et al. (2012)'s boundary formulation. Here, α is the inclination of the infinite slope. Best fit lines were selected to pass through the origin.

The workflow of `GEOSPH`, is as follows: The domain of interest is discretized into SPH particles, surrounded by boundary particles, and a list of nearest neighbor particles in the support domain of each particle is created using a linked list based sorting algorithm. Next, the SPH particles are relaxed under gravity making use of a damping term such that a geostatic state of stress is achieved, and the particles reach their equilibrium positions. `GEOSPH` is a displacement driven code, so a prescribed velocity is applied to the boundary particles. Alternatively, the boundaries can be fixed. From the particle velocities, the velocity gradients and then the deformation rate tensors for each particle are found. A constitutive update is subsequently performed, and the stresses are integrated at each particle using an implicit return mapping algorithm for the Drucker-Prager model described in Borja (2013), which is modified to preserve objectivity in the presence of large deformations by way of the Jaumann stress rate. The integration of the stresses at each particle makes SPH a fully collocational method, in contrast to FEM for example, where the constitutive update is performed at the Gauss points while the displacement field is determined at the nodes. With knowledge of the stresses, the discretized version of the conservation of momentum equation is now solved, and from it, the particle velocities and displacements are computed via a variation of the forward Euler scheme to then march the simulation forward in time. More details on the exact equations solved and the SPH discretization process can be found in our previous paper (del Castillo et al., 2021).

4. Benchmarking

Both analogue and numerical sandbox-style modeling has historically suffered from low reproducibility and difficulty in comparing different modeling results due to variability in modeling materials, numerical methods, or constitutive relations, as well as due to the natural heterogeneity of analogue modeling materials. The works by Buiter et al. (2006) and Buiter et al. (2016) created useful benchmark tests for both shortening and extensional experiments, standardizing the simulation dimensions, material parameters, boundary conditions, etc., while the companion papers of Schreurs et al. (2006) and Schreurs et al. (2016) have sought to accomplish the same with analogue experiments. In Buiter et al. (2006) and Buiter et al. (2016), various different numerical codes perform the same benchmarking experiments and are evaluated against each other. Some of the codes mentioned in Buiter et al. (2006) include (to name a few): `Microfem` (Fullsack, 1995) an ALE FEM code solving the Stokes equations for incompressible flows; `LAPEX-2D` (Babeyko et al., 2002) a Lagrangian finite difference code; `PFC2D` (Itasca, 1999) a DEM code; `I2ELVIS` (Gerya and Yuen, 2007) a finite difference staggered grid marker-in-cell code solving the Stokes equations with visco-elastoplastic or viscoplastic constitutive models. Moreover, in Buiter et al. (2016) the following numerical codes were evaluated: `Eflen` a Lagrangian FEM code solving the conservation of momentum equation (Rockfield, 2017); `Gale` an FEM-particle-in-cell code also solving the Stokes equations; `Sdvig` an FEM code solving the Stokes equations; `I3VIS` the successor code and similar to `I2ELVIS`; and in both Buiter et al. (2006) and Buiter et al. (2016), `Sopale`, an ALE FEM code that solves the conservation of momentum equation. With the exception of `Eflen`, which uses the SR3 elastoplastic constitutive model based on critical state soil mechanics, the other codes use Mohr-Coulomb to capture plastic behavior.

We perform three different benchmarking tests in this study. The stable wedge experiment from Buiter et al. (2016) (Section 4.1), the shortening experiment from Buiter et al. (2006) (Section 4.2), and the S-point experiment from Buiter et al. (2016) (Section 4.3). The setups for these benchmarking experiments are visualized in Figure 2 along with their respective dimensions. We qualitatively compare the structural styles from our results against those of the aforementioned codes in both papers as well as against reported analogue experiments from Schreurs et al. (2006) and Schreurs et al. (2016). Additionally, we make quantitative comparisons in terms of topographic slopes and the location and orientation of thrusts that form in the various wedges in the aforementioned works.

Quartz sand is the principal material component of the sandboxes, which we simulate as an elastoplastic material with a density of $\rho = 1560$ kg/m^3, a cohesion of $c = 10$ Pa, an angle of internal friction of $\phi = 32°$, an angle of dilation of $\psi = 0°$, a Young's Modulus of $E = 5,000$ kPa, and a Poisson's ratio of $\nu = 0.3$. In the shortening experiment, a layer of weak glassy microbeads is used. We assign the microbeads the same parameters as the quartz sand, except with a decreased internal friction angle of $\phi = 21°$. As described in Section 3, the boundaries have a static friction of $\phi_b = 0.79\phi$, which corresponds to $\phi_b = 25.3°$ when quartz sand is in contact with the boundary particles. The chosen values of the material properties are based on those used in Buiter et al. (2006) and Buiter et al. (2016) to facilitate comparison of our results, and are summarized in Table 1 alongside some other useful simulation parameters. We note that although the density of the quartz sand is initially assumed to be constant throughout the sandbox, once the stresses are initialized in the simulations, the sand is compacted and the density will be nonuniform, increasing with depth. In this way, the effects of sand packing are considered. The small but non-zero cohesion value ($c = 10$ Pa) for the quartz sand in our simulations is based on the measured cohesion of quartz sands used in the analogue experiments of Schreurs et al. (2006). Sand and other geologic materials dilate inelastically during failure, but the degree of dilatancy of the material depends on the level of deformation. Particularly, in areas of very high deformation, the angle of dilation rapidly decreases from its initial value to zero (Roscoe and Burland, 1968). Because the sandbox domain in our simulations is subjected to large deformations, the adopted angle of dilation of $\psi = 0°$ is reasonably justified since in the Drucker-Prager model the dilatancy angle is assumed constant, and a constant non-zero value will lead to continuous expansion of the domain. While the chosen cohesion value is accurate for quartz sands, we may expect the cohesion to be higher in other analogue materials such as clays which more accurately model certain orogens in the field (Graveleau et al., 2012). A parametric study showing the effect of varying dilatancy angle and cohesion is included in the Appendix for the accretionary wedge shortening benchmark experiment.

4.1. Preliminary Stable Wedge Experiment

The stable wedge experiment proposed by Buiter et al. (2016) consists of pushing a two-dimensional plane-strain wedge of sediment particles with initial surface slope $\alpha_i = 20°$ across a flat surface ($\beta = 0°$) that is stable according to critical taper theory. Note the previously discussed material properties chosen for the particles (tabulated in Table 1) were selected to represent sand typically used in sandbox experiments. The wedge is pushed for a distance of 4.0 cm by a mobile wall of boundary particles with constant velocity V. Because the wedge is mechanically stable, it should maintain a constant taper throughout the push and not experience any internal deformation (Buiter et al., 2016). To understand the sensitivity of our simulations to the pushing velocity, we plot the pressure and deformation rate fields of the wedge after the 4.0 cm horizontal displacement for different pushing velocities V in Figure 3. In the same figure, we also plot the colored material layers at the end of the 4.0 cm displacement. Starting off as straight parallel layers, the colored layer or material markers are commonly used in sandbox-style experiments to help visualize deformation patterns and can be thought of as different colored strata, as they carry no differing material properties and thus have no mechanical significance. It has been noted that the

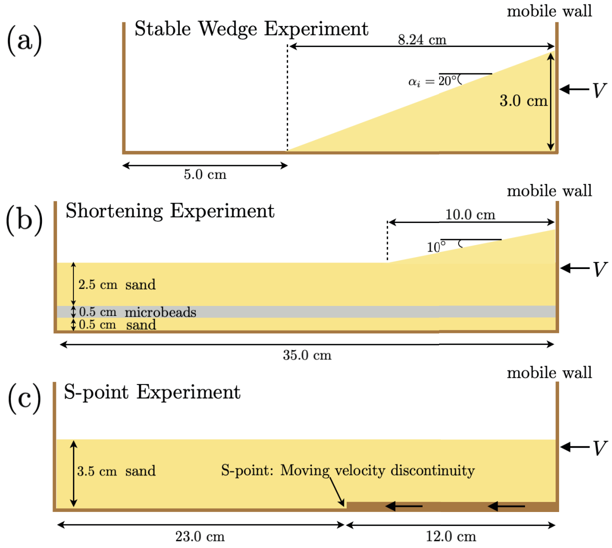

Figure 2: Setups of benchmarking tests. (a) Stable wedge, (b) Shortening experiment, and (c) S-point experiment.

dynamic nature of SPH creates a strong rate-dependency in the solutions with respect to the loading or pushing velocity applied to boundaries. Wang et al. (2019) found that for strain rates less than 0.1 s^{-1}, quasi-static solutions can be achieved, greatly reducing the effect of strain rate (or the pushing velocity). The pushing velocities V selected in the series of tests performed ($V = 0.2, 0.1, 0.01$, and 0.001 cm/s), all have corresponding equivalent strain rates less than 0.1 s^{-1}.

Table 1
Material parameters used throughout the `GEOSPH` simulations unless otherwise specified.

Parameter	Value
Density, ρ [kg/m^3]	1,560
Particle mass, m [kg]	0.0024375
Time step, Δt [s]	3.3×10^{-6}
Initial inter-particle distance, Δ [cm]	0.125
Poisson's Ratio, ν	0.3
Young's Modulus, E [kPa]	5,000
Artificial viscosity parameters, α_π and β_π	1.0
Cohesion, c [Pa]	10
Angle of dilation of sand, ψ [°]	0
Angle of internal friction of sand, ϕ [°]	32
Angle of internal friction of microbeads, ϕ [°]	21
Angle of internal friction of base, ϕ_b [°]	25.3
Pushing velocity, V [cm/s]	0.01

In addition, we also evaluate the performance of the simulations at different pushing rates quantitatively using the measures employed by Buiter et al. (2016). For the plane-strain wedge of domain Ω, the internal rate of dissipation of energy $\dot{W}_i$ is defined as

$$\dot{W}_i = \frac{1}{2} \int_{\Omega} (\boldsymbol{\sigma} : \boldsymbol{d})\, \mathrm{d}\Omega \tag{14}$$

where $\boldsymbol{d} = \left(\boldsymbol{l} + \boldsymbol{l}^T\right)/2$ is the rate of deformation tensor and $\boldsymbol{l} = \partial \boldsymbol{v}/\partial \boldsymbol{x}$ is the velocity gradient tensor. The gravitational rate of work $\dot{W}_g$ is calculated with

$$\dot{W}_g = -\int_{A} (\rho g_y v)\, \mathrm{d}A \tag{15}$$

where A is the area of the wedge, g_y and v are the components of $\boldsymbol{g}$ and velocity in the y direction, respectively. Lastly, the root-mean-square velocity v_{rms} is found using

$$v_{rms} = \sqrt{\frac{1}{A} \int_{A} (u^2 + v^2)\, \mathrm{d}A} \tag{16}$$

where u is the magnitude of velocity in the x direction. Because there should be no internal deformation in the wedge, the deformation rate $\boldsymbol{d}$ equals zero, and so the rate of change of internal energy is $\dot{W}_i = 0$. Furthermore, we would also expect the gravitational rate of work to equal zero, $\dot{W}_g = 0$, since there should be no vertical motion given that the surface slope is constant, and the root-mean-square velocity v_{rms} should be equal to the applied velocity V. These quantities are displayed throughout the duration of the simulations for varying V in Figure 4.

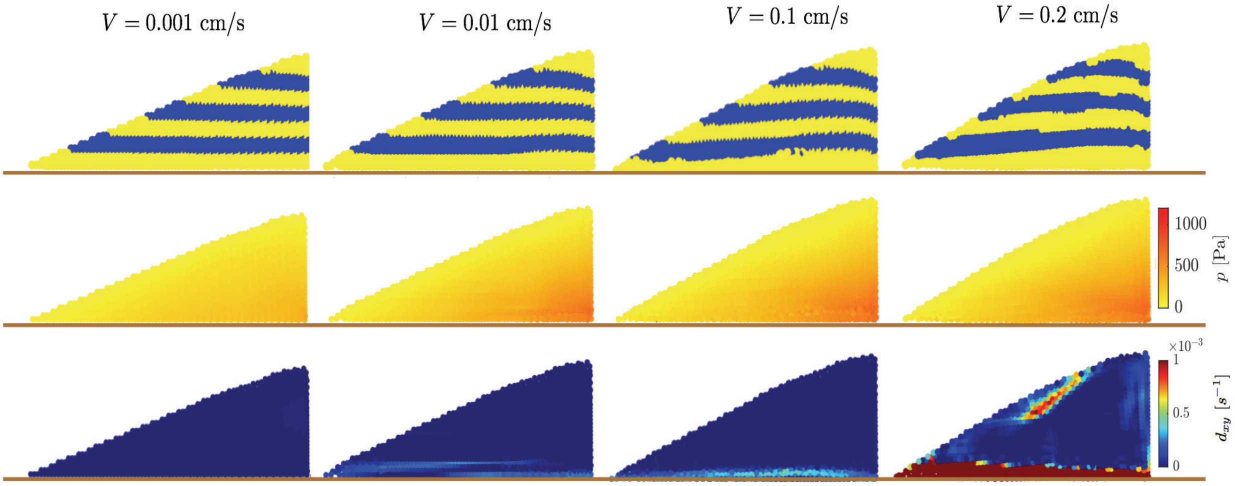

Figure 3: From the stable wedge experiment, material markers (first row), pressure (second row) and shear deformation rate fields (third row) are plotted for varying pushing velocities V after 4.0 cm of shortening. The material markers are purely for the purpose of visualizing deformation within the wedge and the different colors do not represent any material or mechanical distinctions.

From Figures 3 and 4, it is evident that the different measured fields and quantities exhibit a rate dependency with respect to the pushing velocity V. Overall, as V decreases, the magnitudes of the shear deformation rate d_{xy} and the pressure field $p = \mathrm{tr}[\boldsymbol{\sigma}]/3$ decrease, as well as the amount of deformation qualitatively visualized by the thinned, bent, and rotated final configurations of the colored layers in the wedge as seen in Figure 3. Furthermore, the internal rate of dissipation of energy $\dot{W}_i$, and the gravitational rate of work $\dot{W}_g$ decrease with slower V, and approach the expected value of zero. Lastly, the root-mean-squared velocity v_{rms} most closely matches the pushing velocity V as is expected, for slower V. Likewise, in the case of the topographic or surface slope angle α, the ultimate α obtained at the end of the 4 cm push is closest to the expected initial $\alpha_i = 20°$ for slower pushing rates V. For all subsequent simulations in this paper, a pushing velocity of $V = 0.01$ cm/s is considered satisfactory and used going forward, as it balances computational efficiency and accuracy of the results.

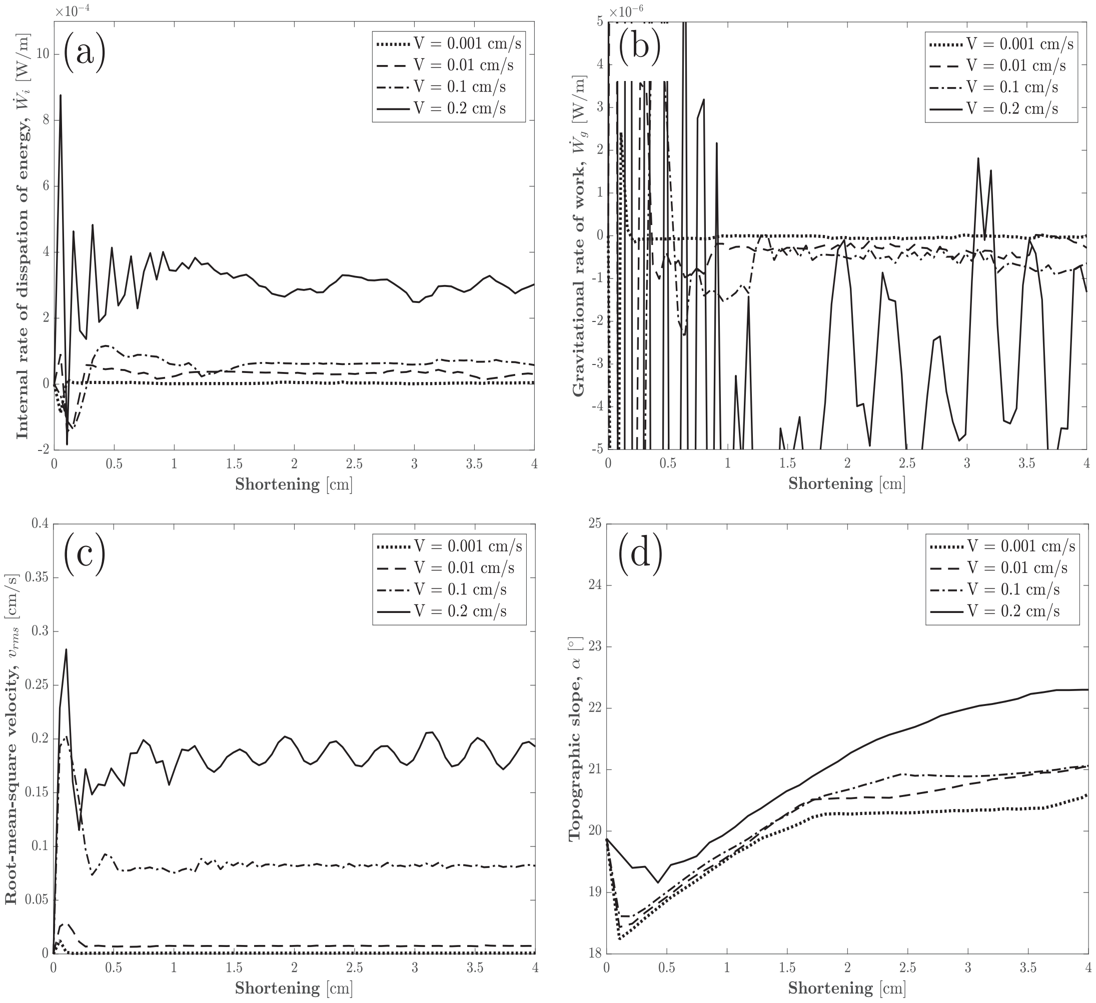

Figure 4: The internal rate of dissipation of energy $\dot{W}_i$ (a), the gravitational rate of work $\dot{W}_g$ (b) the root-mean-square velocity v_{rms} (c), and the topographic or surface slope angle α (d) are plotted with respect to shortening (distance the wedge is pushed) for various pushing velocities V.

4.2. Accretionary Wedge Shortening Experiment

The accretionary wedge shortening benchmark experiment from Buiter et al. (2006) is a classic setup for simulating the formation of a thrust or accretionary wedge (for example see also the works of Davis et al. (1983); Burbidge and Braun (2001); Morgan (2015)), where a 35 cm long by 3.5 cm deep layer of quartz sand ($\phi = 32°$) surrounded by walls is compressed or shortened by moving a mobile wall at a constant velocity V (see Figure 2 (b)). Like in the stable wedge experiment we take $V = 0.01$ cm/s, and the walls are all discretized as boundary particles. In total, approximately 8700 particles are used to discretize the sandbox system. Along the mobile wall, there is a pre-existing formed sand wedge which is 10 cm long and has a slope of 10°, and 0.5 cm above the base there is a 0.5 cm deep layer of microbeads. The microbeads have an internal friction angle of $\phi = 21.0°$, but otherwise have the same properties as the quartz sand. The inclusion of a weak material layer in the sand pack in the form of microbeads has the practical effect of serving as an agent for carrying the deformation forward and promoting the propagation of thrusts. The weak layer is intended to represent an intermediate detachment layer above the basal décollements typically consisting of weaker evaporites or shales as observed in a number of locations worldwide such as the Zagros of Iran (Nilfouroushan et al., 2012), the Northern Apennines of Italy (Massoli et al., 2006), or the Canadian Rocky Mountains (Stockmal et al., 2007).

In Figure 5, snapshots from the shortening experiments are shown at different amounts of horizontal contraction. The maximum shortening achieved is 14.0 cm, in line with the procedure of Buiter et al. (2006). Figure 5 (a), shows colored material layers to highlight the deformation patterns occurring in the wedge, particularly forward thrusting. As seen in Figure 5 (b), the weak microbead detachment initially sustains higher amounts of plastic strain than the neighboring quartz sand, and it is here where strain localization occurs first. Beginning by 1.0 cm and ending by 6.0 cm shortening, the first thrust propagates from the microbead detachment rather than from the basal décollement, close to the mobile wall at the bottom right corner of the model, connecting with a cluster of strain localization at the top surface near the kink in topographic slope. As shortening continues, more forward thrusts propagate from the microbead detachment layer, with an occasional backthrust. The majority of the backthrusts also experience far lower accumulated plastic strains than do the forward thrusts. An exception to this rule is a backthrust forming at the top right of the model which propagates downwards to the microbead detachment. This backthrust may be caused in part by stress concentrations resulting from the boundary conditions along the backstop native to SPH, which do not prevent frictional slip along this interface. Similar backthrusts along the backstop were observed in certain simulations in Buiter et al. (2006) which also did not prevent friction along the backstop, or in some of the analogue experiments of Schreurs et al. (2006), as it is generally very difficult to avoid friction along the backstop in analogue setups (Graveleau et al., 2012). Overall, qualitatively, the wedges produced by `GEOSPH` closely resemble those reported in Buiter et al. (2006), particularly using the `LAPEX-2D`, `Sopale`, and `I2ELVIS` codes.

Because of the velocity discontinuity along the mobile wall at the bottom right corner, high pressure $p = \mathrm{tr}[\sigma]/3$ is achieved (see Figure 6 (a)). On the other hand, in panel (b), the deviatoric (or von Mises) stress q given by $q = \sqrt{3J_2}$ is also highest in the bottom right corner and in the region surrounding the weak microbead detachment, but is relatively lower in the detachment itself. The vertical component of the velocity field v, is highest above the microbead detachment, and shows how the sand behaves rigidly sliding upwards along the shear band or thrust fault planes. In panel (a), superimposed over the pressure field p are vectors indicating the directions of the maximum

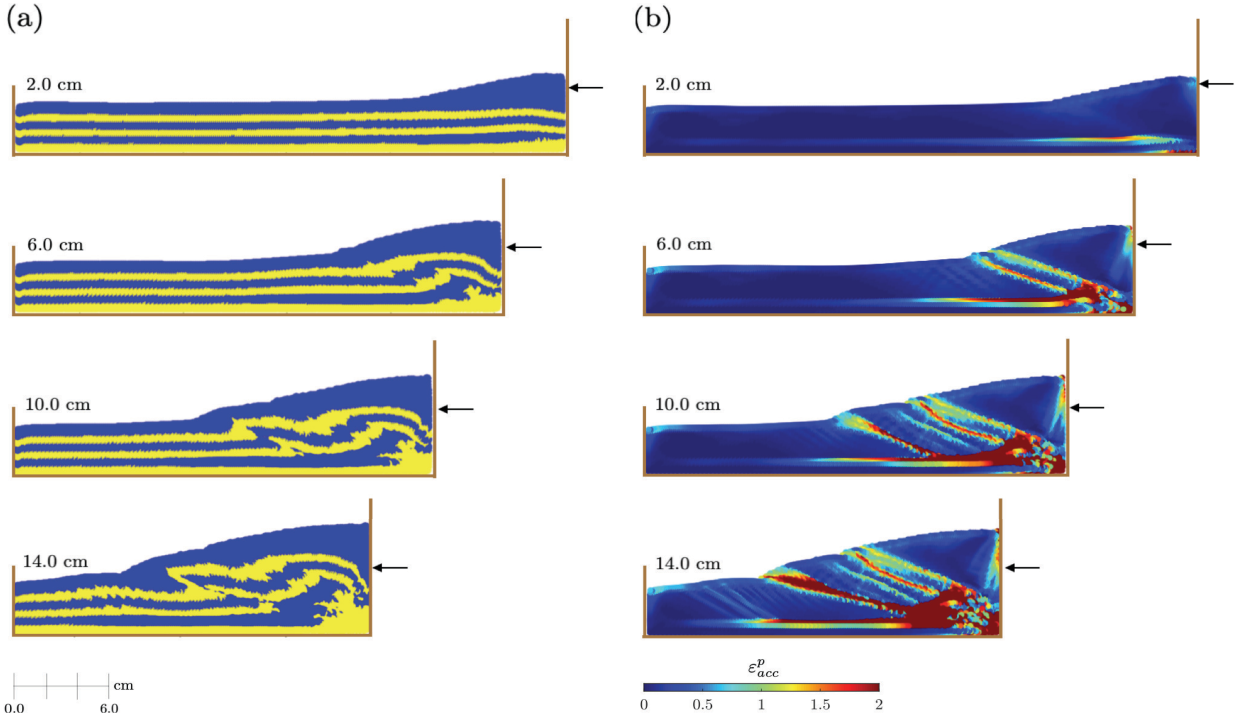

Figure 5: Snapshots of the shortening experiments. On the left in (a) colored material layers are plotted for different amounts of shortening, and on the right in (b), contours of the accumulated plastic strain ε^p_{acc} are plotted. The accumulated plastic strain is calculated by time integrating the norm of the plastic deformation rate tensor $\|\boldsymbol{d}^p\|$.

principal stress σ_1. In the sand preceding the wedge toe, the direction of σ_1 is horizontal, whereas within the wedge σ_1 points in a direction roughly parallel to the inclined surface of the wedge. The average orientation of σ_1 within the wedge with respect to the base closely matches the prediction given by Ψ_b, from critical taper theory. There is considerable heterogeneity in the direction of σ_1 within the wedge however, and the direction of σ_1 is deflected across the shear bands, where they undergo a mild rotation.

We also compare our SPH results against those of the Buiter et al. (2006) codes in a quantitative way by looking at the variation of the topographic slope α throughout the duration of the simulation, as well as the location and orientation of the thrusts or shear bands. In Figure 7, we plot α obtained from the SPH simulations up to the maximum 14.0 cm shortening against the topographic slopes of the codes from Buiter et al. (2006) and from the analogue sandbox experiments from the companion paper of Buiter et al. (2006), Schreurs et al. (2006). We also plot the expected maximum and minimum topographic slopes predicted by critical taper theory as horizontal dashed lines, for the basal frictions prescribed in the different codes and experiments. Note those in Buiter et al. (2006) and Schreurs et al. (2006) had a $\phi_b = 19.0°$, while that in `GEOSPH` was determined to be $\phi_b = 25.3°$.

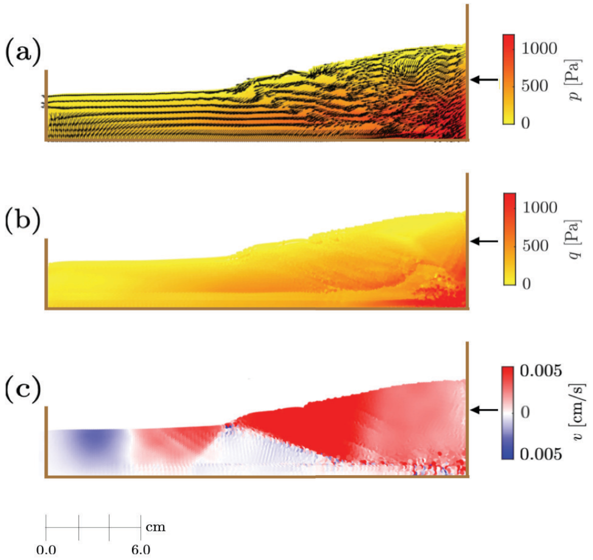

Figure 6: In (a) the vectors at every 3 particles indicate the direction of σ_1 plotted superimposed over the pressure p field. In (b) the von Mises stress q field and in (c) v, the vertical component of velocity are plotted, respectively. Plots are shown after 10.0 cm shortening.

Alongside the `Sopale`, `I2ELVIS`, and `LAPEX-2D` results, `GEOSPH` produces topographic angles α close to the bottom range of the angles produced by the analogue experiments. Furthermore, by 14.0 cm of shortening, the topographic slope of the wedge closely approaches the minimum critical taper value.

In Figure 8, the dip angles of the thrusts with respect to the base are plotted in (a) comparing the results of our SPH simulations against the numerical results of Buiter et al. (2006) and the analogue experiments of Schreurs et al. (2006). In dashed lines we display the theoretical predictions for the orientations of the thrusts with respect to the maximum principal stress σ_1 direction given by the Roscoe angle $\Theta_R = 45° - \psi/2$ (Roscoe, 1970), Arthur angle $\Theta_A = 45° - (\phi + \psi)/4$ (Arthur et al., 1977), and Coulomb angle $\Theta = 45° - \phi/2$ (Coulomb, 1776) for shortening experiments (passive loading condition). However, since these theoretical predictions are with respect to σ_1, and we measure the fault dip with respect to the horizontal, while from Figure 6 (a), σ_1 is not parallel to the horizontal within the wedge, we must correct the predictions for the angles by the factor of Ψ_b (Equation 2) from critical taper theory, which is the analytical prediction for the orientation of σ_1 with respect to the base. For the material parameters used in the simulations, $\Psi_b = 14.23°$. Note that the first three thrusts form within the wedge itself so Θ_A, Θ_R, and Θ_C for the first three thrusts are lower than for the next four thrusts by Ψ_b. The dip angles of the thrusts from our simulations agree well with the benchmarks, and overall are closest to the predictions from the Arthur angle. This result is consistent with the orientations of shear bands produced in a simpler problem setup,

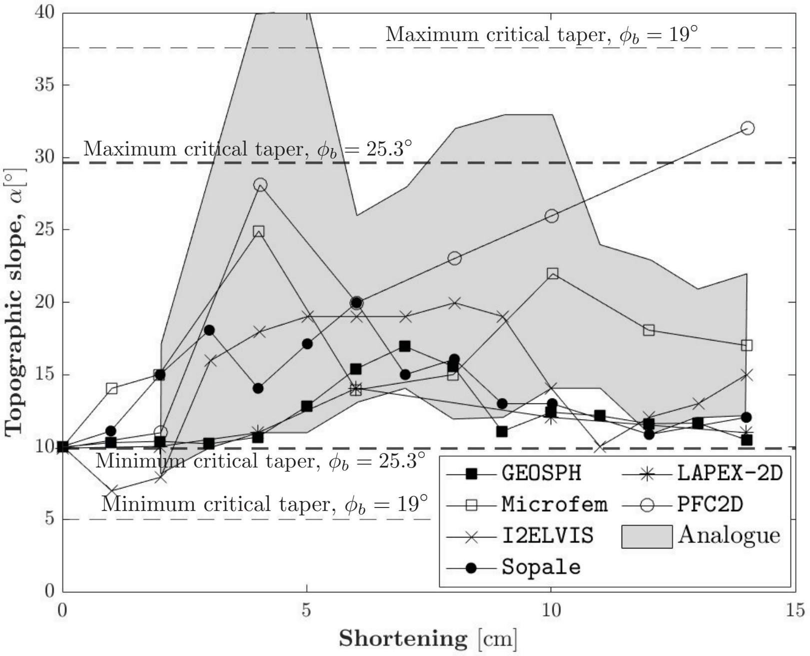

Figure 7: Variation of the topographic slope with shortening distance for the benchmarking accretionary wedge shortening experiment. The results of `GEOSPH` are compared against those from the numerical simulations of Buiter et al. (2006) and the analogue experiments of Schreurs et al. (2006).

that of a backfill behind a retaining wall using our same SPH formulation and constitutive model (del Castillo et al., 2021).

In panel (b) of Figure 8, the amount of shortening at which each thrust propagates in the SPH simulations is again compared against the values of Buiter et al. (2006) and Schreurs et al. (2006). Initially, the amount of shortening required for each thrust remains constant up to thrust 4, but subsequently after, this amount of shortening decreases, and the thrust spacing is less for the last two thrusts. These results agree well with the benchmarking experiments.

As a final check of our SPH simulation results we further evaluate our simulated topographic slopes (tapers) against those predicted by the critical taper solutions at different décollement dips β in Figure 9. For this purpose, shortening simulations with $\beta = -5, 5, 10, 15, 20°$ are performed in addition to $\beta = 0°$, and the varying décollement dips are achieved by tilting the direction of the gravity vector accordingly. Note for these simulations the layer of microbeads is removed and the entire wedge is made of quartz sand, to more accurately compare against the critical taper solutions which assume a constant internal angle of friction ϕ. In addition to these simulations, which have a basal friction angle of 25.3°, we experiment with a method to change the effective basal friction by adding a weak material layer of 0.5 cm height with prescribed internal friction $\phi = 10°$, similar to the microbead layer, but this time directly facing the bottom basal boundary. This procedure, similar to that employed by Simpson (2011), shifts the décollement upwards to the interface between the microbead and quartz sand layers providing an effective basal friction angle of $\phi_b = 10.0°$ for the entire wedge. To ensure that simulated wedges with this setup take the tapers

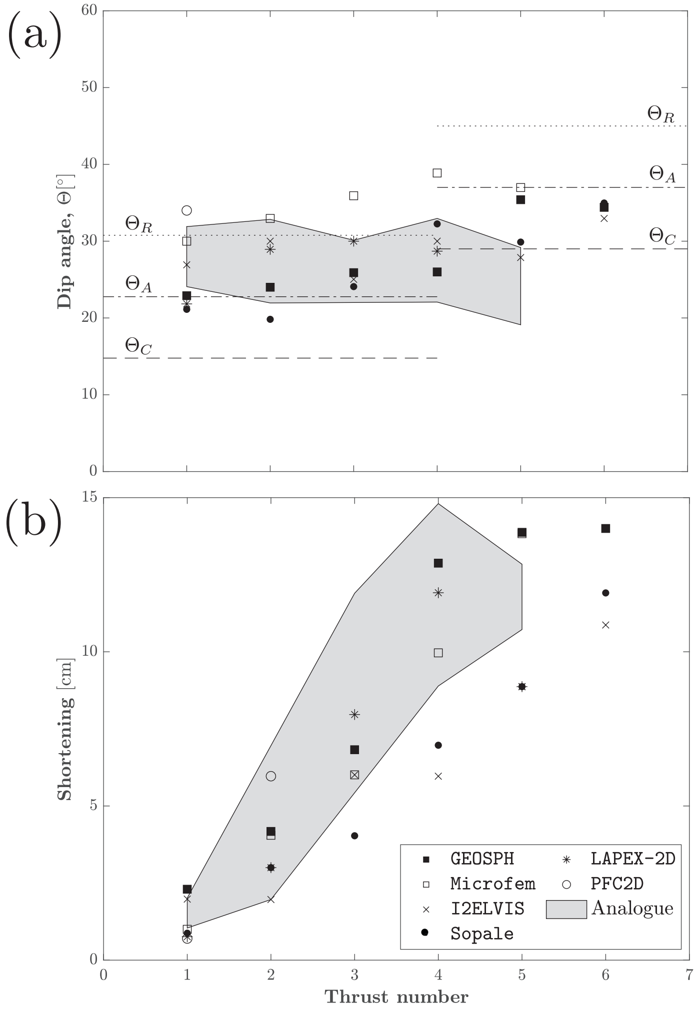

Figure 8: The dip angles of thrusts or shear bands ordered as they emerge are shown in panel (a), while in (b) the amount of shortening required for each particular thrust to fully propagate is shown.

(or topographic slopes) predicted by critical taper theory given $\phi_b = 10.0°$, like in the $\phi_b = 25.3°$ case, we similarly perform shortening experiments for varying décollement dips.

The tapers measured from the SPH simulations of accretionary wedges closely follow the critical taper analytical solutions for both values of the basal friction. This result indicates that adding the weak layer with $\phi = 10.0°$ along the base succeeds in designating an effective basal friction angle of $\phi_b = 10.0°$ for the wedge.

4.3. S-point Experiment

The problem setup of the S-point experiment based on that of Buiter et al. (2016) consists of a 35.0 cm long by 3.5 cm high quartz sand layer that is pushed by a mobile wall attached to a thin basal film running along the length of the base for a total length of 12.0 cm all of which is pushed at a velocity V. The complex of basal film and mobile wall is denoted the mobile backstop or backstop, and the thin basal film is modeled as a continuation of the boundary walls and in the

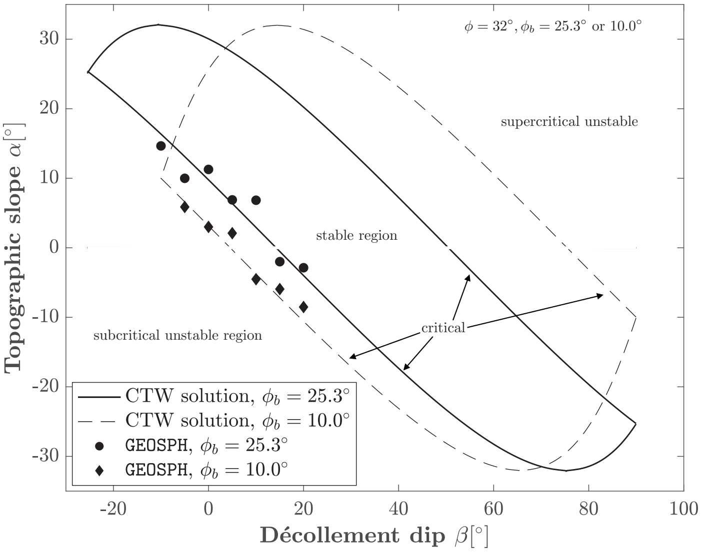

Figure 9: Measured tapers from accretionary wedge shortening simulations with varying β using $\phi_b = 25.3°$ or $\phi_b = 10.0°$ after 14.0 cm shortening compared against the critical taper solutions for each respective basal friction value.

SPH discretization is 2 boundary particles in height. The tip of the basal film thus represents a moving velocity discontinuity denoted as the S-point. Differing from the experimental setup of Buiter et al. (2016) where the backstop is rigid and a basal film drags the sand to the S-point, here the backstop indents the sand layers, like in the setup of Wang and Davis (1996). Other studies have indicated that the direction of sand movement does not affect the overall system kinematics or mechanics and that both problem setups are equivalent (Graveleau et al., 2012). The S-point is intended to model the velocity discontinuity that forms during subduction at a convergent margin, although the actual subduction process is omitted in the simplified model, and a doubly vergent wedge forms as the sand layers are shortened (Beaumont et al., 1996).

In Figure 10, colored material layers in column (a) and the accumulated plastic strain ε^p_{acc} in (b) are displayed at various amounts of shortening, until the final simulation shortening of 10.0 cm is reached, according to Buiter et al. (2016). Initial strain localization occurs early on after 1.0 cm shortening at the S-point parallel to the base, and by 2.0 cm, diffuse conjugate shear bands propagate from the S-point to the surface, and refine as shortening progresses. The forward vergent (pointing in the direction of shortening) band forms first and is quickly followed by the backward vergent one. By 2.0 cm shortening, significant surface uplift between the bands can be observed, and this continued uplift forms an initial pop-up structure. As more forward vergent bands form they are pushed upwards and by 10.0 cm a distinct doubly vergent wedge has formed. Comparing our results qualitatively with the benchmarks of Buiter et al. (2016), initial localization is observed roughly after the same amount of shortening and only one main backward vergent band or thrust forms. After 10.0 cm shortening, however, the final configuration of the doubly vergent wedge resembles those of the sandbox experiments from the companion paper Schreurs et al. (2016) more than those from various of the numerical codes in Buiter et al. (2016) some of which produce multiple pop up structures in front of the main doubly vergent wedge rather than just the doubly vergent wedge itself. However, like some of the numerical codes, the `GEOSPH`-produced wedge lacks the completely flat surface of the axial zone seen in many of the sandbox experiments.

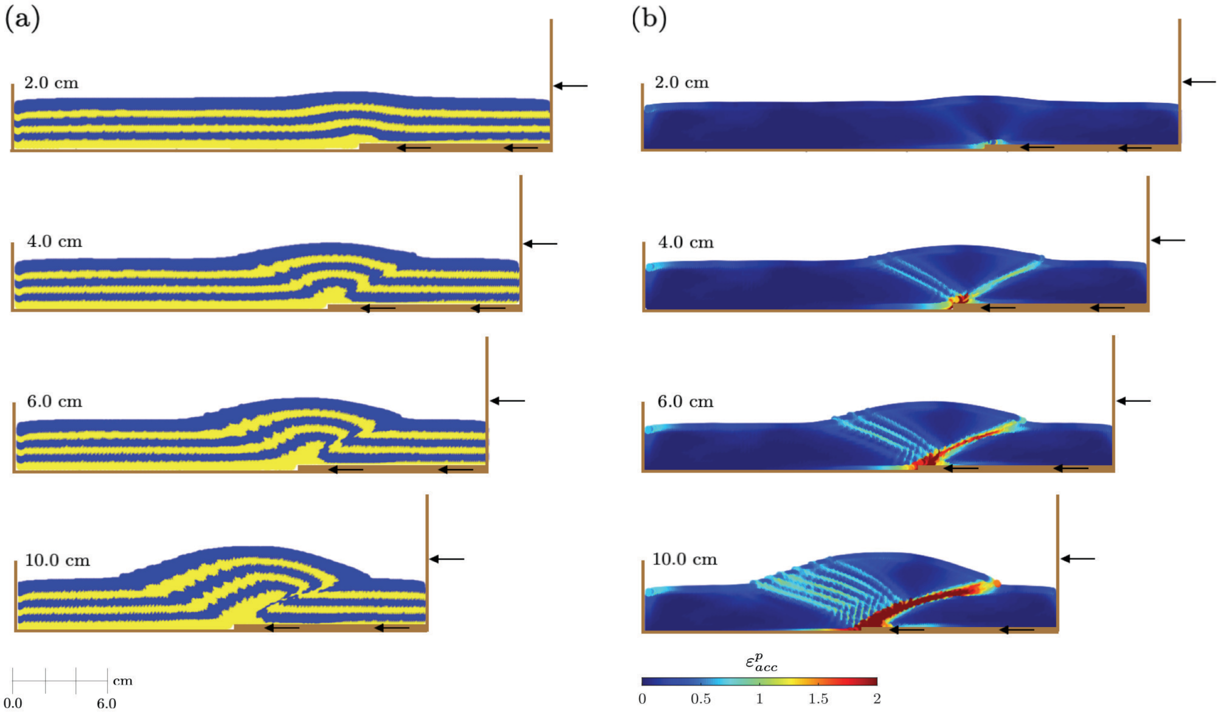

Figure 10: Snapshots of the S-point experiment at different amounts of shortening. (a) deformation patterns, and (b) accumulated plastic strain.

The anatomy of a doubly vergent wedge can be divided into three primary regions, the prowedge, i.e., the doubly vergent wedge toe pointing in the direction of shortening, the retrowedge, the toe of the doubly vergent wedge pointing in the direction opposite that of shortening, and a relatively flat area of the top surface between prowedge and retrowedge known as the axial zone. Like in the accretionary wedge shortening benchmark experiment, the direction of σ_1 is parallel to the surface or horizontal in the sand in front of the S-point and doubly vergent wedge, while in the prowedge it is mostly inclined with respect to the top surface as is the case in the retrowedge, and the directions are altered and rotated across shear bands (see Figure 11 (a)). However, in the axial zone, σ_1 points vertically downwards, especially close to the surface. The significant downwards vertical σ_1 direction is compounded with great upwards vertical motion as seen by the plot of v in panel (c) and results in horizontal extension along the axial zone. The von Mises stress q in panel (c) once again shows that it is highest in the vicinity of initial shear band nucleation close to the S-point.

We also compare the topographic slopes of the prowedge α_p from our simulations against those of various codes used in Buiter et al. (2016) and the analogue experiments of Schreurs et al. (2016). We note that both analogue and numerical benchmarks used a lower basal friction of $\phi_b = 14.0°$,

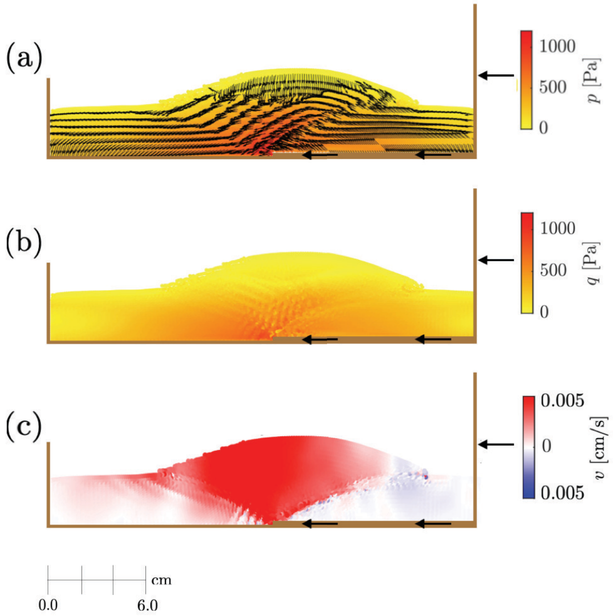

Figure 11: For the S-point experiment, in (a) the vectors at every 3 particles indicate the direction of σ_1 plotted superimposed over the pressure p field. In (b) the von Mises stress q field and in (c) v, the vertical component of velocity are plotted, respectively. Plots are shown after 10.0 cm shortening.

and so we compare the results against the critical taper solutions for both corresponding basal frictions. The `GEOSPH` α_p values closely follow those of the analogue experiments and along with all the other experimental results, numerical or analogue, the prowedge slopes do not approach the critical taper solutions after 10.0 cm shortening (see Figure 12). It remains unclear, however, if the prowedge topographic angle or the retrowedge topographic angle should be at the values prescribed by critical taper theory, the angle of repose, or some value lower than both of these. Because of the significant vertical uplift of newly formed thrusts or forward vergent shear bands, the presence of a retrowedge and an axial zone, the radically different directions of the maximum principal stress σ_1, and the lack of clarity regarding which surface should be the décollement, application of the critical taper model to doubly vergent orogens is a subject of debate (Buiter et al., 2016). In Section 5.1, a model of double the length of the original S-point experiment (70.0 cm long) is considered to see if after additional shortening, either the prowedge topographic angle α_p or the retrowedge topographic angle α_r approach the critical taper predictions or the angle of repose for the material parameters used in the simulation.

In Figure 13, the dip angles of the forward vergent shear bands or forward thrusts are plotted in the left panel for each one that emerges, and the backward vergent bands or backward thrusts are shown in the right panel. The dips are measured at the top of the band close to the surface,

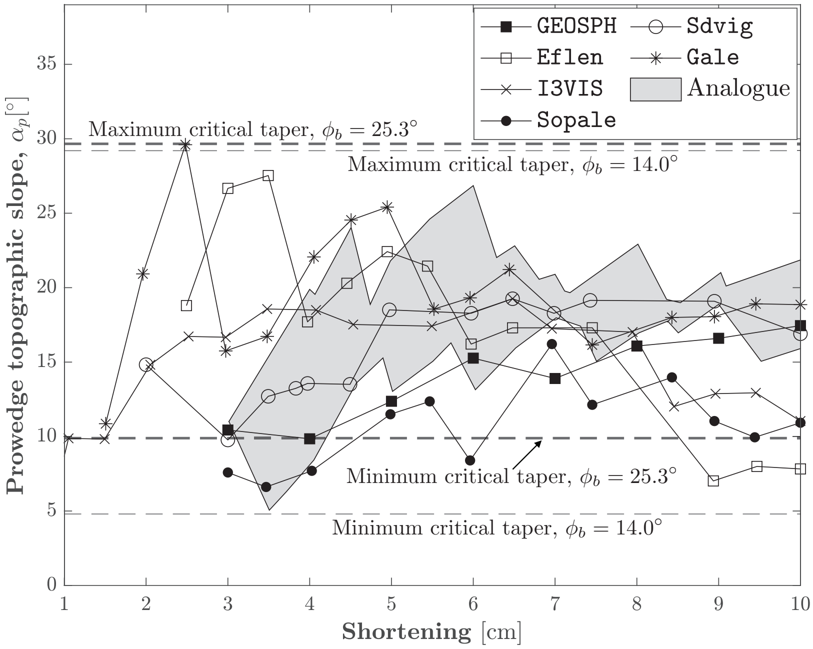

Figure 12: Variation of the prowedge topographic slope with shortening distance for the benchmarking S-point experiment. The results of `GEOSPH` are compared against those from the numerical simulations of Buiter et al. (2016) and the analogue experiments of Schreurs et al. (2016).

and immediately after the thrusts or bands form and propagate to the surface, to avoid the back rotation and uplifting of the bands as shortening proceeds. The `GEOSPH` values generally agree well with those of the numerical codes from Buiter et al. (2016) in both cases, and for the forward thrusts show that the first thrusts take the Arthur orientation Θ_A and gradually become shallower, approaching a Coulomb orientation Θ_C over continued shortening.

5. Discussion

5.1. Double Length S-point Experiment

As mentioned in Section 4.3, explaining the slopes of the prowedge and retrowedge of doubly vergent wedges using critical taper theory faces considerable theoretical hurdles. Nevertheless, in the sandbox experiments of Wang and Davis (1996), the prowedge topographic slope converged to the minimum critical taper topographic slope, while the retrowedge slope achieved a value below the maximum critical taper value, and the angle of repose. A similar result was observed in the FEM simulations of Simpson (2011). Willett et al. (1993) and Willett (1999) observed that α_p was oriented at the minimum critical taper, while the retrowedge side ultimately obtained a kinked slope with the top half at the maximum taper angle, and the second part towards the toe at the minimum taper. The works of Koons (1990), Bonini et al. (1999), Storti and Salvini (2000), Persson (2001), Soto et al. (2006), among others, however, noted the deficiencies of the critical taper model in predicting the topographic slope of the prowedge, and found that the dominant mechanical process

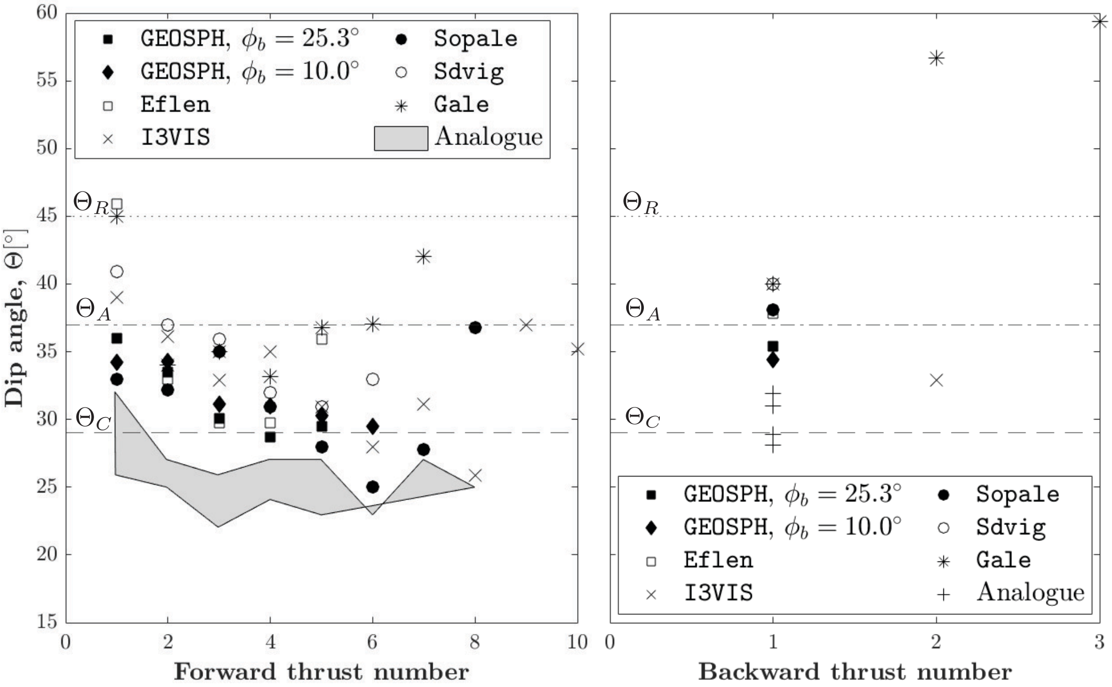

Figure 13: The dip angles of thrusts or shear bands ordered as they emerge in the S-point experiment. In the left panel, the forward vergent thrusts are shown, and on the right, the backward vergent thrusts are displayed.

in retrowedges was not thrusting or gravity spreading but rather shallow mass wasting or slope failure, with α_r at the angle of repose.

To investigate the variation of the slopes α_p and α_r beyond 10.0 cm shortening like in Figure 12, we use an S-point experiment setup with double the length of that of Buiter et al. (2016) to allow for shortening of up to 30.0 cm without any interference from the rigid wall at the far end of the model setup (see Figure 14 (a)). We also consider a second model setup with a weak 0.5 cm deep layer above the base with $\phi = 10°$, giving the model a basal friction of $\phi_b = 10°$, to compare the effect of varying the basal friction (see Figure 14 (b)). In Figure 15, the slopes of α_r and α_p for the original $\phi_b = 25.3°$ and the $\phi_b = 10.0°$ models are plotted up to 30.0 cm shortening. The analogue experimental results of Schreurs et al. (2016) are included up to 10.0 cm for reference, as are the maximum and minimum critical taper values and the angle of repose.

From our results in Figure 15, the prowedge topographical angle α_p does not approach the critical taper values, and instead takes a value close to $\alpha_p = 19.0°$ in the $\phi_b = 25.3°$ case, and $\alpha_p = 7.0°$ in the $\phi_b = 10.0°$ case. The retrowedge slopes α_r, approach the angle of repose but do not ultimately reach its inclination, instead being closer to the maximum critical taper values. However, there is no evidence of any thrusts or of the distinctive strain localization patterns of progressive failure and gravity spreading which would be expected if the retrowedge were forming at the maximum critical taper, and instead, there seems to be considerable amount of debris at the toe of the retrowedge suggesting the retrowedge slope is an exclusive product of shallow slope failure. We return to this issue in greater detail at the end of the next subsection.

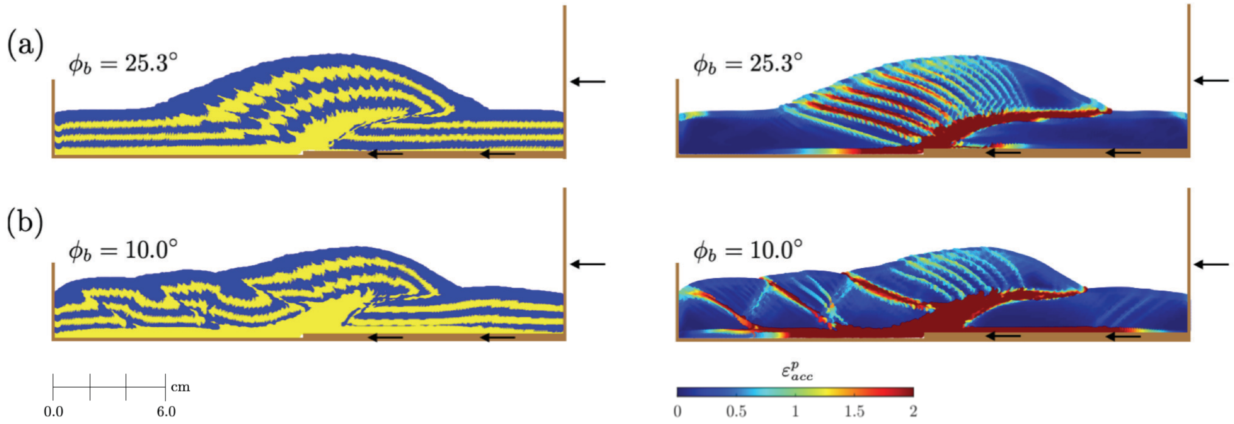

Figure 14: In (a) and (b), the colored material layers and ε^p_{acc} are displayed for the $\phi_b = 25.3°$ and $\phi_b = 10.0°$ double length S-point simulations respectively at 30.0 cm shortening.

5.2. Role of Varying Backstop Geometry in Forearc Basins

The doubly vergent wedges emerging from the S-point experimental setup are best suited for modeling systems forming as a result of continental collision or in active margins when both plates have the same material properties and there is no region of stronger or more rigid material acting as an indenter (Beaumont et al., 1996). However, in many active margins, continental crust or plates experience varying strength and rigid indenters compressing weaker sediment may be present. In volcanic forearcs, strong volcanic basement rock forming a backstop compresses weaker sediment located just forward of the backstop, forming a doubly vergent wedge. In the indenter modeling framework, as noted by Persson (2001), the S-point experimental setup is actually a special case of an indentation experiment where the indenter and the indented sediment layers have the same material properties. In fact, we observe that a natural indenter forms in the sand layers before the S-point velocity discontinuity as the area behind the S-point is relatively undeformed and behaves rigidly (see Figure 14 (a)).

Byrne et al. (1993) pointed out that from reflection seismic profiles, three clear types of backstop indenter geometries could be observed. In the first, denoted Type I (see Figure 16 (a)), the backstop is inclined pointing in the forward direction, and the toe of the backstop lies along the décollement plane. With this positioning of the backstop, the backstop scrapes or plows through the forward lying weak sediment causing it to accrete above the backstop. The type I backstop is the most commonly observed in nature, found for example in the Lesser Antilles (Byrne et al., 1993), the Alps indented by the Adriatic plate (Bonini et al., 1999), the Urals (Persson, 2001), and

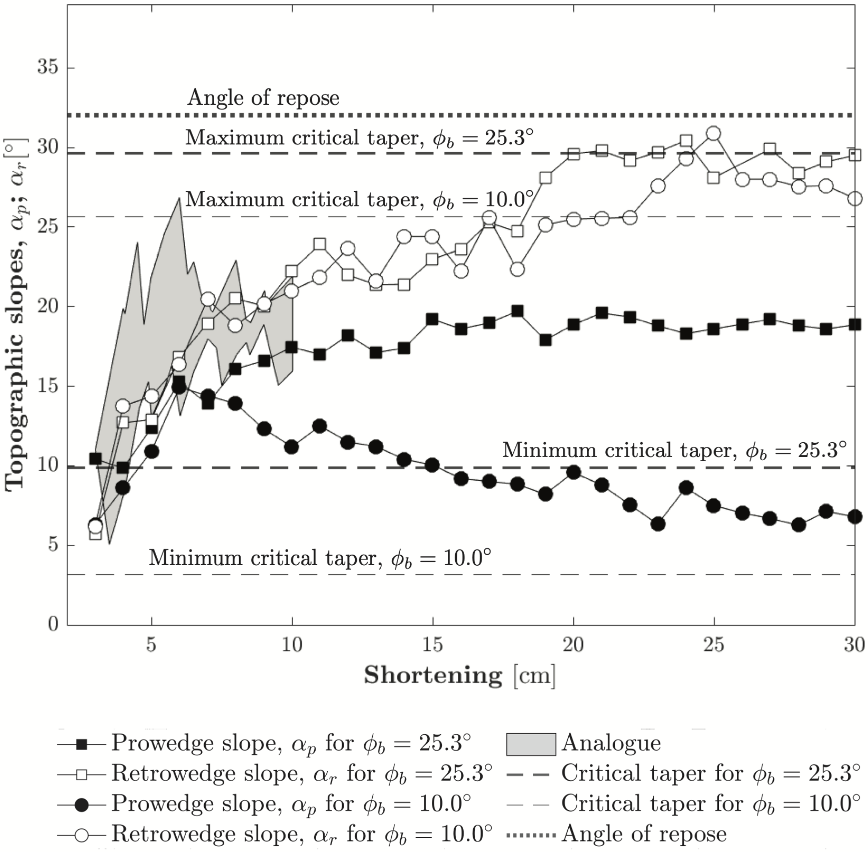

Figure 15: The variation of the prowedge and retrowedge topographic angles for the double length S-point simulations is shown up to 30.0 cm shortening, and compared with the critical taper values.

also produces the most visible and cleanest accretion patterns. For these reasons, studies of type I backstops have been most prevalent in the literature. The work of Persson (2001) and Bonini et al. (1999) found that the inclination of the type I backstop caused profound structural differences in the doubly vergent wedges. For inclinations greater than 45°, the foreshear and retroshear bands did not propagate from the tip of the indenter, or the S-point, the location of the velocity discontinuity, and rather propagated from a location they labeled the P-point, located slightly further forward than the tip of the indenter. Therefore, the area between the S and P-points was considered an effective indenter, or simply being pushed along by the indenter in the backstop, as if it were a part of it. For inclinations less than 15°, Persson (2001) and Bonini et al. (1999) found that the S and P-points matched in location, but that this time an effective indenter formed above the backstop, while for inclinations between 15° and 45°, the S and P-points matched in location, and no effective indenter formed, so the retroshear band hugged the backstop indenter.

In the type II indenter, the indenter is also inclined pointing forwards, but inverted with respect to the type I indenter, and the toe of the indenter is located significantly above the décollement leading to underthrusting of weak sediment (and some accretion above too) as the backstop advances. The type III indenter consists of a taper-shaped wedge geometry, located with its toe at an intermediate depth. Examples of type II and type III indenters include the Vancouver Island convergent margin, and the Peru margin respectively (Byrne et al., 1993).

Byrne et al. (1993) conducted a series of coarse FEM simulations using the von-Mises yield criterion and determined that doubly vergent wedges should form in all three backstop types, regardless of the significant underthrusting expected in types II and III. However, their analysis did not realistically recreate the shape of doubly vergent wedges observed in seismic profiles, balanced cross section reconstructions, or in sandbox experiments. Furthermore, their simulations could not accurately predict the paths of strain localization within the wedges. The sandbox experiments of Bonini et al. (1999) and Persson (2001) suffered from this same limitation, and tracked the formation of shear bands using offsets in the colored material marker layers of the sand. We recreate the simulations of Byrne et al. (1993) using inclinations of the backstop indenter from each of the three regimes identified by Persson (2001) and Bonini et al. (1999) (15°, 30°, and 75°) and with the advantage of the SPH method which easily provides not only colored material markers as do sandbox experiments, but also detailed strain and strain rate fields.

In Figures 16 and 17, the results with different indenter geometries for simulations with $\phi_b = 25.3°$ and $\phi_b = 10.0°$ are plotted respectively after 30.0 cm shortening. Here we show the colored material layers in panel (a) and the accumulated plastic strain ε^p_{acc} in panel (b). In Figure 18 we show snapshots in different moments in time of the volumetric deformation rate d_{vol} and the vertical component of the velocity v. Shear bands are intermittent and undergo an active phase when initially forming where they exhibit high strain rates, so we plot the volumetric deformation rate in panel (a) to show the instantaneous active shear banding as opposed to the accumulated plastic strain which shows the historical deformation of the material. In panel (b) we plot the vertical component of the velocity field v, which together with d_{vol} helps us to determine the shape of the effective indenters in our simulations. We determine the effective indenters to be areas near the backstop indenter with close to zero v behaving rigidly, and that are bounded by continuously active shear banding. We display the effective indenters (E.I.) in Figure 18 as the area delimited by black circular dots.

Overall, doubly vergent wedges form in all cases of backstop geometry types and inclinations, like in the work of Byrne et al. (1993). Furthermore, in the type II and to a lesser extent in the type III backstop types, also like in the simulations of Byrne et al. (1993), the material being underthrusted beneath the backstop undergoes high amounts of deformation as quantified by the accumulated plastic strain.

The doubly vergent wedges forming in the original S-point experiment most closely resemble those from the type I backstop at 30° inclination experiment. The S-point experiment can be thought of as generating a roughly 30° inclined natural indenter, as the material behind the retroshear band is mostly undeformed, and acts rigidly. A notable difference between the S-point experiment and the rigid 30° type I backstop is that the natural indenter of the former is subject to deformation and shear banding, while in that of the later, it is made of boundary particles, and thus no shear banding or faulting can occur.

Additionally, like in the results of Bonini et al. (1999) and Persson (2001), three main regimes are observed for the type I backstop, that of inclinations between 0° and 30°, between 30° and 45°, and lastly for inclinations between 45° and 90°. In the 15° and 30° simulations for type I, the S and P-points match. However, we note that in the 30° case a very thin effective indenter forms along the inclined plane of the rigid indenter, which was not detected in the sandbox experiments of Bonini

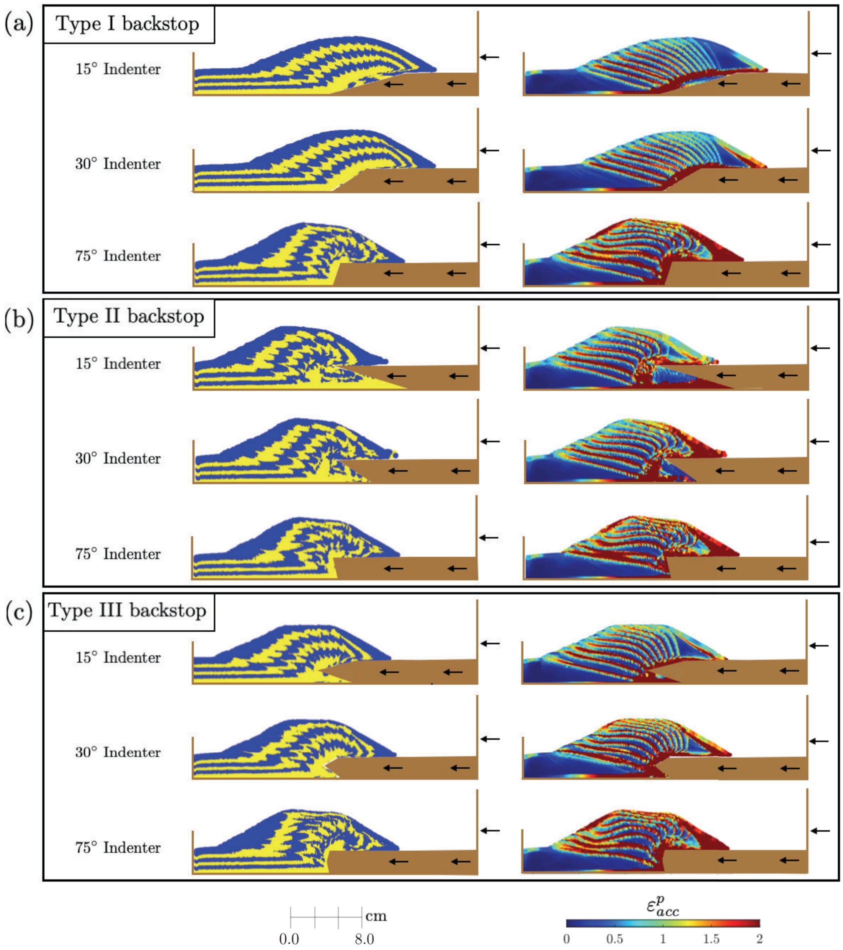

Figure 16: For the $\phi_b = 25.3°$ simulations, colored material layers are shown in the left column, and contours of the accumulated plastic strain are displayed in the right column after 30.0 cm shortening for the three different backstop types and inclinations of the indenter.

et al. (1999) and Persson (2001) (see Figure 18 panel a).

We also observe that the structural styles of the shear bands and material layers of the type II and type III experiments for the $\phi_b = 25.3°$ case (Figure 16) highly resemble that of the 75° type I case, with significant vertical motion of the sand causing distortion of the uplifted shear bands, extensional faulting in the axial zone of the wedge, and steep slopes on the pro side, occasionally close to the angle of repose along the top half. In all three inclinations of the type II backstop, (only 15° is shown in Figure 18 (a) for brevity) the effective indenter takes the inclination of 70°, which is close to the inclination of the effective indenter in the 75° inclination type I setup, which is 62°. This steep effective indenter in the type II experiments, regardless of the inclination of the actual backstop indenter itself, leads to the large vertical uplift of the sand and a doubly vergent wedge resembling that of the type I case with an inclination of 75°. In the type III backstops, the inclination of the effective indenter depends on the inclination of the actual backstop indenter. For a backstop indenter inclination of 15°, the effective indenter has an inclination of 40°; for a backstop indenter of 30°, the effective indenter has an inclination of 45°; and for 75°, the effective indenter

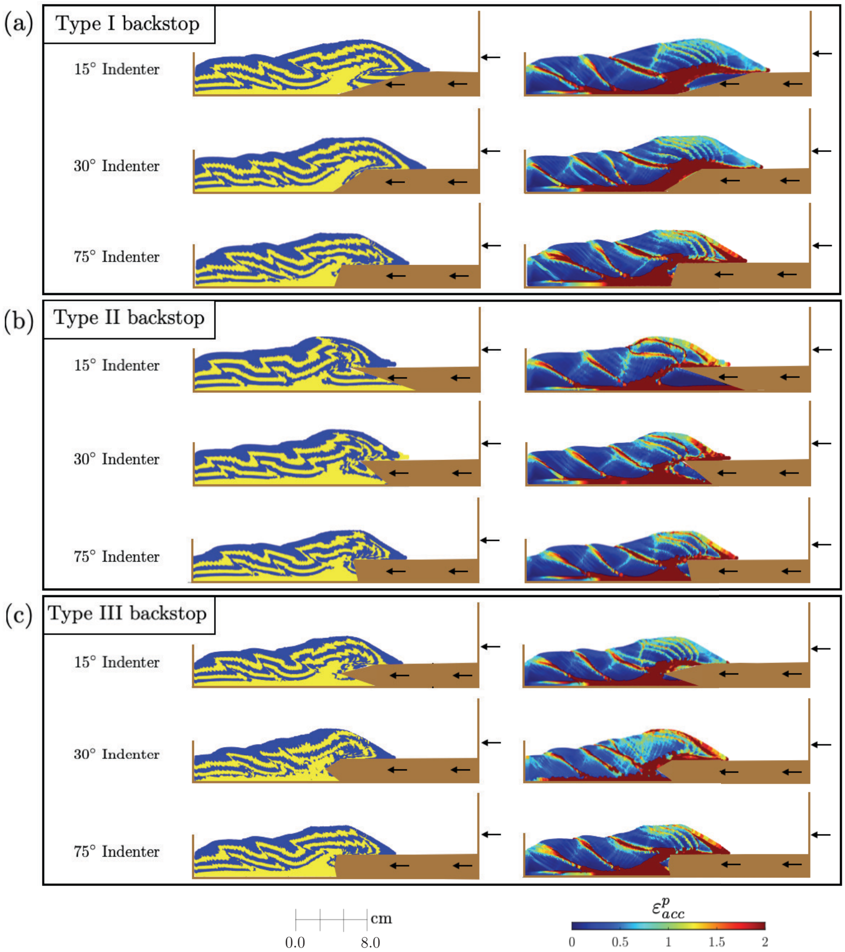

Figure 17: For the $\phi_b = 10.0°$ simulations, colored material layers are shown in the left column, and contours of the accumulated plastic strain are displayed in the right column after 30.0 cm shortening for the three different backstop types and inclinations of the indenter.

has an inclination of 67°.

While in the type I backstop for inclinations of 15° and 30°, shear bands propagate from the P-point, which overlaps the S-point, for the 75° inclination case, shear bands initially form at the top left corner of the indenter and propagate downwards until reaching the base where they then reflect forming forward vergent bands or thrusts. The reflected forward verging bands are occasionally active alongside the original backward vergent band forming a conjugate pair, or alternatively, can also be active alone. We also note that in the simulations with type I backstops of 15° and 30° inclination, the main backshear band is continuously active throughout the duration of the simulation. A similar occurrence is observed in all type II simulations, where the bands propagate from the top-most forward corner of the indenter. In the type III backstops, for inclinations of 15° and 30°, the shear bands form at the mid-height furthest forward point of the indenter, while in the type III backstop inclined at 75°, the bands propagate from the top-most corner like in the type II and the 75° inclined type I simulations.

In the simulations with a lower basal friction of $\phi_b = 10°$ (see Figure 17), similar effective

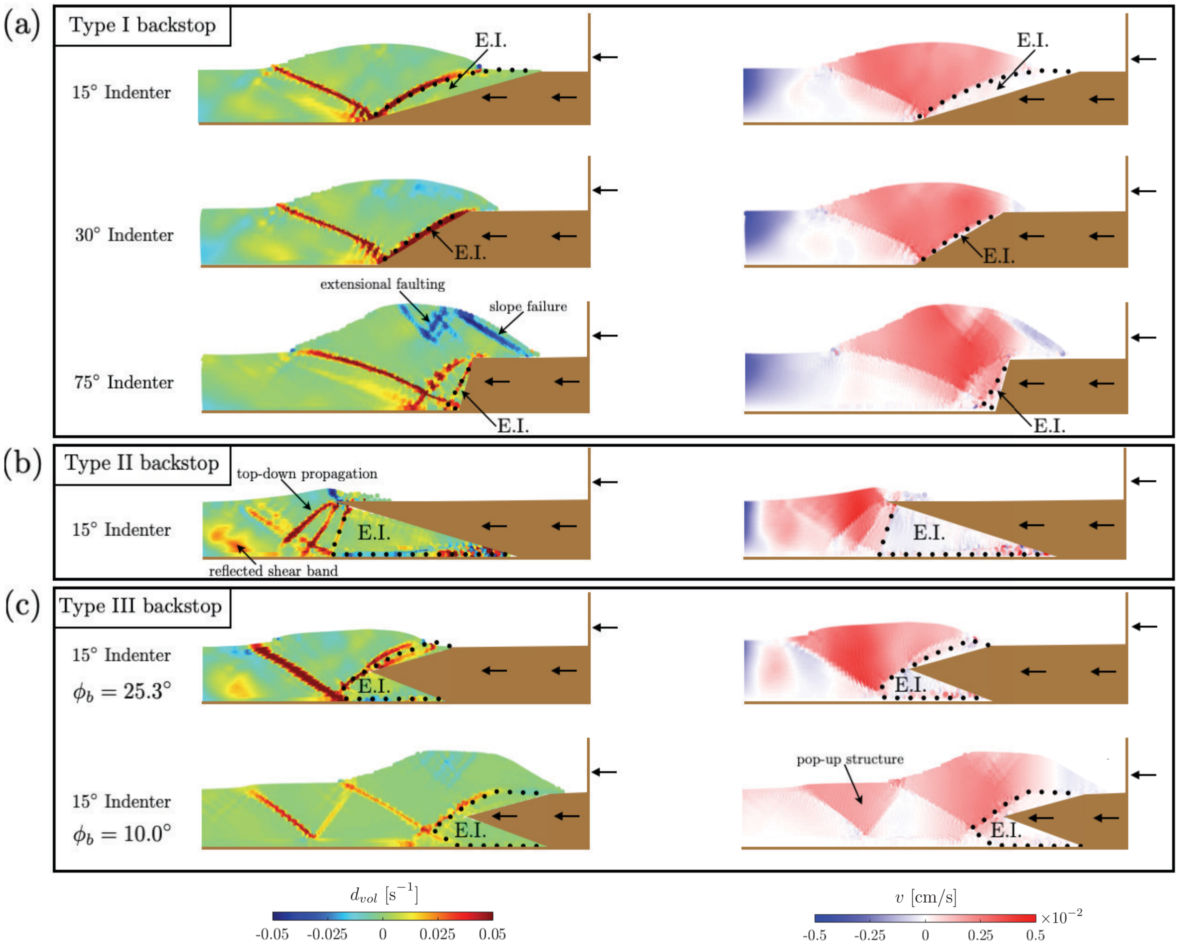

Figure 18: In the left column the volumetric deformation rate d_{vol} and in the right column the vertical component of the velocity v are displayed for different indenter inclinations and backstop types to identify the various effective indenter (abbreviated as E.I.) shapes, and shear band propagation and deformation patterns. All simulations use $\phi_b = 25.3°$ except the last type III 15° indenter with $\phi_b = 10.0°$. Note the panels represent snapshots in time corresponding to different amounts of shortening to highlight the patterns we seek to illustrate. The first and second rows are shown after 4.25 cm shortening, the third after 9.25 cm, the fourth after 2.0 cm, the fifth after 4.5 cm, and the sixth after 12.0 cm.

indenter inclinations form, indicating that these are a product of the backstop indenter shape and inclination, not of any basal properties. However, the weaker base has the effect of carrying deformation forwards, and while the initial shear banding pattern is similar to the $\phi_b = 25.3°$ simulations, conjugate shear bands subsequently form from the weak basal layer resulting in consecutive pop-up structures (see Figure 18 panel c). From Figure 17 (b), the forward vergent pair accumulates more plastic strain than the retro vergent over the course of 30.0 cm shortening. The addition of a weaker basal layer shallows the prowedge topographic slopes ranging from 7.5° to 10.8°, but they are still greater than the expected minimum critical taper values, while the retrowedge slopes ranging from 28.0° to 30.6° lie between the angle of repose and the maximum critical taper angle (see Table 3). In the $\phi_b = 25.3°$ models, the slopes for the prowedge after 30.0 cm shortening vary between

Table 2
Prowedge and retrowedge topographic slopes α_p and α_r after 30.0 cm indentation for the $\phi_b = 25.3°$ model.

Indenter type	α_p [°]	α_r [°]
S-point	18.9	29.5
type I, 15° inclination	20.1	29.6
type I, 30° inclination	22.0	31.4
type I, 75° inclination	28.3	31.9
type II, 15° inclination	26.7	31.5
type II, 30° inclination	27.0	30.5
type II, 75° inclination	28.0	31.2
type III, 15° inclination	25.6	30.2
type III, 30° inclination	26.0	31.0
type III, 75° inclination	29.0	31.5

Table 3
Prowedge and retrowedge topographic slopes α_p and α_r after 30.0 cm indentation for the $\phi_b = 10.0°$ model.

Indenter type	α_p [°]	α_r [°]
S-point	6.8	26.8
type I, 15° inclination	7.5	28.0
type I, 30° inclination	8.3	28.0
type I, 75° inclination	8.5	29.0
type II, 15° inclination	9.0	30.2
type II, 30° inclination	8.8	29.7
type II, 75° inclination	10.5	30.4
type III, 15° inclination	8.2	30.0
type III, 30° inclination	10.0	30.5
type III, 75° inclination	10.8	30.6

20.1° and 29.0° (see Table 2) which is significantly above the minimum taper angle but still below the maximum taper angle, while the retrowedge slopes vary between 29.6° and 31.9° closer to the angle of repose of 32°.

The topographic slopes from the prowedges and retrowedges suggest that critical taper theory does not describe the geometry of doubly vergent wedges particularly well. As seen from our simulations, forward thrusting is not the only deformation mechanism within the doubly vergent wedges, as uplift due to the ramp-like indenter, and slope failure along the wedge flanks, also occur on both retro and pro sides. In the retrowedge, slope failure is observed continuously as seen from the shallow logarithmic spiral-like failure surfaces, and a zone of debris with very high accumulated plastic strain resulting from these slope failures gathers above the rigid backstop indenter at the toe of the retrowedge. Slope failure is also visible in the prowedge of every type II and III indenter simulation as well as in the type I indenter with an inclination of 75° case, roughly after 10.0 cm of shortening whenever the local surface slope near the top of the prowedge approaches the angle of repose. In the prowedge, forward thrusting actually reduces the topographic angle, because the thrust sheets (or occasionally pop-up structures), which are uplifted slightly as material accretes, force the prowedge to grow horizontally, thus having the effect of shallowing the surface slope of the entire prowedge. In the $\phi_b = 10.0°$ simulations where forward thrusting is facilitated by the weak base, thrusting dominates, and slope failure is seldom seen as the prowedge slope is never close to the angle of repose at any point. These observations suggest that forward thrusting and vertical uplift as a result of the indentation process act as opposing forces, in turn reducing and increasing the prowedge slope angle α_p respectively, with shallow slope failure manifesting itself whenever vertical uplifting presides over forward thrusting to ensure the slope never exceeds the angle of repose.

In traditional accretionary or thrust wedges, forward thrusting maintains the wedge taper at the minimum critical taper. In a doubly vergent wedge, however, the presence of vertical uplift due to the indenter leads to prowedge tapers that are considerably greater than the minimum critical taper, as the effect of forward thrusting is generally insufficient to produce prowedge tapers predicted by critical taper theory. At the same time, in the retrowedge, we also do not observe strain localization patterns characteristic of progressive failure and gravity spreading, which are the mechanisms by which a wedge usually achieves the maximum critical taper (Dahlen, 1984; Mourgues et al., 2014), whereas we do see continuous shallow slope failure. This suggests that the topographic slope of the retrowedge with values generally lying between the maximum critical taper and the angle of repose, is purely a product of slope failure, occurring whenever the retrowedge slope locally exceeds the angle of repose. It is also important to note that the inclination of the indenter plays an important role as well, as steeper indenters, especially for type I and III backstops, tend to have steeper topographic slopes on both retro and pro sides, and more frequent slope failures over the course of the simulations.

6. Closure

We have applied a meshfree fully Lagrangian smoothed particle hydrodynamics (SPH) code to successfully handle the large deformation and strain localization phenomena of geologic materials in sandbox-style experiments. The SPH method avoids mesh entanglement and the complexities that finite element method (FEM) codes encounter when modeling large scale geodynamic processes, and is also more computationally efficient and scalable than non-continuum meshfree methods such as the discrete element method (DEM), while easily providing continuum level stress, strain, and strain rate information like in FEM simulations. To the authors' best knowledge, this is the first time SPH has been applied to simulate accretionary and doubly vergent wedges using the purely mechanical IBVP and elastoplastic constitutive models, as is routine in simulations using FEM.

In simulations of accretionary wedges and doubly vergent wedges, SPH accurately reproduces results from the benchmarking experiments proposed by Buiter et al. (2006) and Buiter et al. (2016) in terms of overall deformation patterns, topographic slopes, thrust dips, and number of thrusts. In accretionary wedges thrust dips or shear bands are oriented at the Arthur angle $\Theta_A = 45° - (\phi + \psi)/4$, while in doubly vergent wedges, the first few forward vergent thrusts form at the Arthur angle, but as shortening progresses, bands begin to form closer to the orientation of the Coulomb angle $\Theta_C = 45° - \phi/2$. After 14.0 cm shortening, the accretionary wedge taper approaches the minimum critical taper value. Furthermore, in the doubly vergent wedges, we find the retrowedge's topographic slope to be close to the angle of repose and controlled by repeated shallow slope failure, while on the prowedge side, the slope is determined by the competing processes of forward thrusting and vertical uplift caused by the indenter.

In simulations of doubly vergent wedges using a rigid backstop indenter, effective indenters form in the three different backstop types of Byrne et al. (1993) and in the three main inclination groups of Bonini et al. (1999) and Persson (2001). We find that simulations with type II and III backstops generate similar results to simulations with a type I backstop with an inclination of 75°, due to the similar inclinations taken by the type II and III effective indenters to that of type I with an inclination of 75°. The effective indenters are characterized by zones of low deformation in type I and very high deformation in type II and III indenters, that move rigidly, and are delimited by continously active shear bands. It is worth mentioning that in type II and III indenters, we find that shear bands do not form at the P-point but rather at one of the protruding tips of the indenter, then propagate downwards and reflect at the perceived P-point on the basal detachment. This represents a considerably different propagation process than that observed by Bonini et al. (1999) and Persson (2001) with their analogue sandbox experiments.

As mentioned before, one of the limitations of the current work is the inability to control the contrast between the internal angle of friction of sediment particles and of the boundary particles. Improved boundary conditions that capture frictional sliding more accurately, and which are a current ongoing topic of SPH research, should be implemented in future work. For now, the work-around of adding a weak material layer along the base has permitted changing the effective basal friction in the context of critical taper theory. Since most orogenic wedges in the field are not completely dry, but rather have pores filled with water, modeling the effect of pore fluid in conjunction with solid deformation would also be valuable (Zhao and Borja, 2020, 2021; Zhang and Borja, 2021). The Drucker-Prager model may not be appropriate for such condition, and critical state models capable of representing plastic volumetric compaction, such as the family of Cam-Clay models (Semnani et al., 2016; Zhao et al., 2018; Borja et al., 2020; Yin et al., 2021), or other models endowed with a compression cap (Lade and Kim, 1988; Aydin et al., 2006), may be more suitable for representing the buildup of fluid pressures under tectonic compression (Bekins and Dreiss, 1992; Saffer and Bekins, 2002; Cutillo et al., 2003; Saffer and Bekins, 2006; Rowe et al., 2012). From a modeling perspective, simulating more faithful representations of fold-and-thrust systems in three dimensions reconstructed from field data, not just considering the simplified plane-strain wedge case common in sandbox experiments, is worthy of tackling with SPH going forward. Adding the physics of erosion and deposition to our models would also be possible because SPH can capture free surfaces naturally without any additional formulations, and several models to account for strata erosion/deposition adaptable to SPH have been proposed (Zubeldia et al., 2018; Nikooei and Manzari, 2021). Incorporation of some these factors into our models is currently underway.

Acknowledgments

This material is based upon work supported by the U.S. Department of Energy, Office of Science, Office of Basic Energy Sciences, Geosciences Research Program, under Award Number DE-FG02-03ER15454. The support by the National Science Foundation under Award Number CMMI-1914780 is also acknowledged. The first author acknowledges the support by the U.S.

National Science Foundation (NSF) Graduate Research Fellowship under Grant DGE 1656518, as well as by the Stanford Graduate Fellowship.

Appendix

As an additional exercise, a brief parametric study to consider the effects of varying the angle of dilation or the cohesion on the overall wedge geometry and deformation patterns in the accretionary wedge shortening benchmark (Section 4.2) is performed. In the first set of simulations, the angle of dilation is varied from the original value of $\psi = 0°$ to 5° and then to 11°, while keeping all other material parameters, dimensions, setup, etc., the same as in the previously discussed accretionary wedge shortening benchmark experiment. In the second set of simulations, the cohesion value is increased from the original value of $c = 10$ to 50 and then to 100 Pa, while keeping all other parameters unchanged from those of the original benchmark. The simulations varying the angle of dilation are displayed in Figure 19 whereas those varying cohesion are plotted in Figure 20 at two different amounts of shortening.

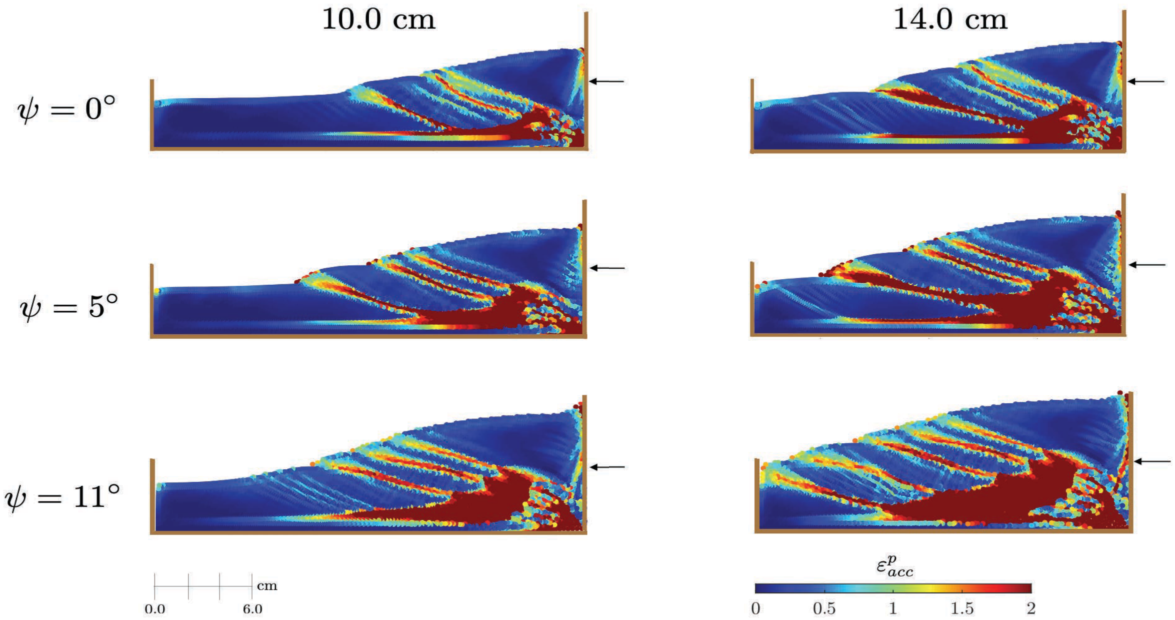

Figure 19: For purposes of a parametric study, the accretionary wedge shortening benchmark simulations from Section 4.2 are performed with varying angles of dilation ($\psi = 0°$, 5°, and 11°), while keeping the setup and other parameters the same as the original benchmark. Snapshots at 10.0 and 14.0 cm shortening are displayed.

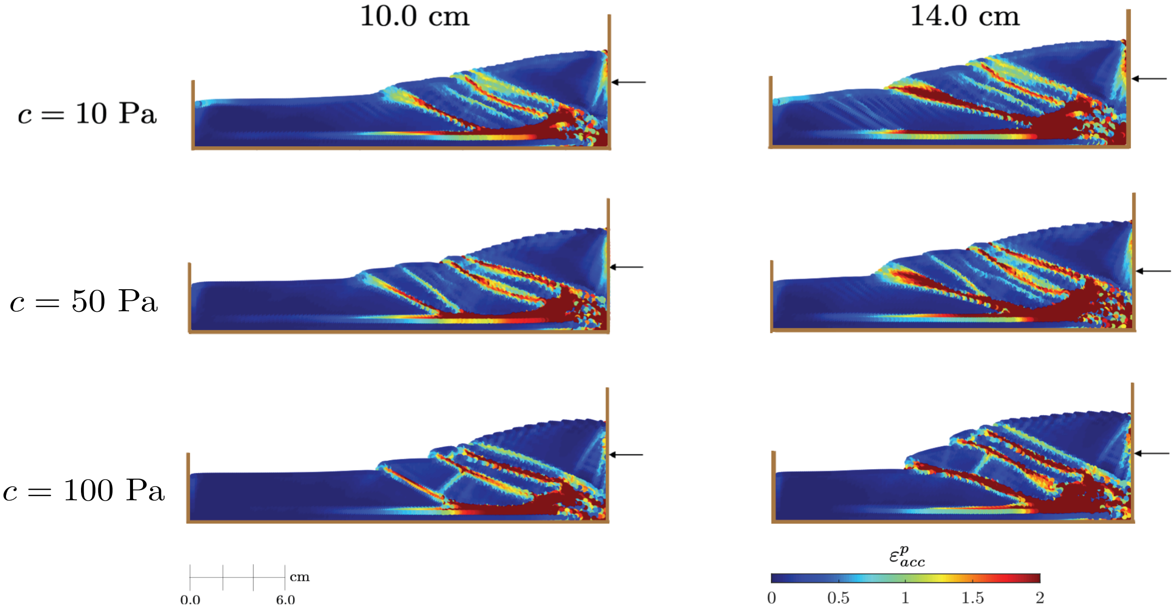

Figure 20: Same as Figure 19, except here simulations are performed with varying cohesion (c =10, 50, and 100 Pa), while keeping all other parameters the same as the original benchmark.

As seen from Figure 19, increasing the angle of dilation results in more extensive volume expansion of the sand. Despite the fact that the sand is being compressed by the shortening, the compressive elastic volume change is offset by the considerably greater plastic dilative volume change, resulting in overall volumetric expansion. The volumetric expansion smoothens the topographic slope, eliminating any protruding sheets caused by propagating thrusts. As seen in the panels in Figure 19, the dilatancy angle cannot be constant, otherwise, the domain will keep on expanding aphysically. For this reason, a zero value of the angle of dilation is preferred for our sandbox simulations undergoing large deformations.

From our parametric study, it is also evident that in simulations with dilatancy angles approaching the friction angle of the soil ($\phi = 32°$), the degree of non-associativity decreases in the plastic flow, rendering less pronounced shear bands. Increasing cohesion as seen in Figure 20, on the other hand, steepens the wedge slope, and enhances the protrusion of the thrust sheets, which concords with other numerical modeling studies (Nilfouroushan et al., 2012; Morgan, 2015). Furthermore, the shear bands become more refined, and regions between the bands undergo less plastic deformation over the course of the simulation.

References

Adami, S., Hu, X.Y., Adams, N.A., 2012. A generalized wall boundary condition for smoothed particle hydrodynamics. Journal of Computational Physics 231, 7057–7075.

Albertz, M., Sanz, P.F., 2012. Critical state finite element models of contractional fault-related folding: Part 2. Mechanical analysis. Tectonophysics 576-577, 150–170.

Arthur, J.R.F., Dunstan, T., Al-Ani, Q.A.J.L., Assadi, A., 1977. Plastic deformation and failure in granular media. Géotechnique 27, 53–74.

Aydin, A., Borja, R.I., Eichhubl, P., 2006. Geological and mathematical framework for failure modes in granular rock. Journal of Structural Geology 29, 83–98.

Babeyko, A.Y., Sobolev, S.V., Trumbull, R.B., Oncken, O., Lavier, L.L., 2002. Numerical models of crustal scale convection and partial melting beneath the Altiplano-Puna plateau. Earth and Planetary Science Letters 199, 373–388.

Beaumont, C., Ellis, S., Hamilton, J., Fullsack, P., 1996. Mechanical model for subduction-collision tectonics of Alpine-type compressional orogens. Geology 24, 675–678.

Bekins, B.A., Dreiss, S.J., 1992. A simplified analysis of parameters controlling dewatering in accretionary prisms. Earth and Planetary Science Letters 109, 275–287.

Belytschko, T., Black, T., 1999. Elastic crack growth in finite elements with minimal remeshing. International Journal for Numerical Methods in Engineering 45, 601–620.

Bilotti, F., Shaw, J.H., 2005. Deep-water Niger Delta fold and thrust belt modeled as a critical-taper wedge: The influence of elevated basal fluid pressure on structural styles. AAPG Bulletin 89, 1475–1491.

Bonini, M., Sokoutis, D., Talbot, C.J., Boccaletti, M., Milnes, A.G., 1999. Indenter growth in analogue models of Alpine-type deformation. Tectonics 18, 119–128.

Borja, R.I., 2000. A finite element model for strain localization analysis of strongly discontinuous fields based on standard Galerkin approximation. Computer Methods in Applied Mechanics and Engineering 190, 1529–1549.

Borja, R.I., 2013. Plasticity Modeling & Computation. Springer-Verlag.

Borja, R.I., Aydin, A., 2004. Computational modeling of deformation bands in granular media, I: Geological and mathematical framework. Computer Methods in Applied Mechanics and Engineering 193, 2667–2698.

Borja, R.I., Dreiss, S.J., 1989. Numerical modeling of accretionary wedge mechanics: Application to the Barbados subduction problem. Journal of Geophysical Research 94, 9323–9229.

Borja, R.I., Regueiro, R.A., 2001. Strain localization in frictional materials exhibiting displacement jumps. Computer Methods in Applied Mechanics and Engineering 190, 2555–2580.

Borja, R.I., Song, X., L.Rechenmacher, A., Abedi, S., Wu, W., 2013a. Shear band in sand with spatially varying density. Journal of the Mechanics and Physics of Solids 61, 219–234.

Borja, R.I., Song, X., Wu, W., 2013b. Critical state plasticity. Part VII: Triggering a shear band in variably saturated porous media. Computer

Methods in Applied Mechanics and Engineering 261-262, 66–82.

Borja, R.I., Yin, Q., Zhao, Y., 2020. Cam-Clay plasticity. Part IX: On the anisotropy, heterogeneity, and viscoplasticity of shale. Computer Methods in Applied Mechanics and Engineering 360, 112695.

Buiter, S.J., Schreurs, G., Albertz, M., Gerya, T.V., Kaus, B., Landry, W., le Pourhiet, L., Mishin, Y., Egholm, D.L., Cooke, M., Maillot, B., Thieulot, C., Crook, T., May, D., Souloumiac, P., Beaumont, C., 2016. Benchmarking analogue models of brittle thrust wedges. Journal of Structural Geology 92, 140–177.

Buiter, S.J.H., Babeyko, A.Y., Ellis, S., Gerya, T.V., Kaus, B.J.P., Kellner, A., Schreurs, G., Yamada, Y., 2006. The numerical sandbox: comparison of model results for a shortening and extension experiment. Geological Society, London Special Publications 253, 29–64.

Burbidge, D.R., Braun, J., 2001. Numerical models of the evolution of accretionary wedges and fold-and-thrust belts using the distinct-element method. Geophsyical Journal International 148, 542–561.

Byrne, D.E., Wang, W.H., Davis, D., 1993. Mechanical role of backstops in the growth of forearcs. Tectonics 12, 123–144.

Cardozo, N., Bhalla, K., Zehnder, A.T., Allmendinger, R.W., 2003. Mechanical models of fault propagation folds and comparison to the trishear kinematic model. Journal of Structural Geology 25, 1–18.

del Castillo, E.M., Fávero Neto, A.H., Borja, R.I., 2021. Fault propagation and surface rupture in geologic materials with a meshfree continuum method. Acta Geotechnica 16, 2463–2486. doi:`https://doi.org/10.1007/s11440-021-01233-6`.

Chandra, B., Singer, V., Teschemacher, T., Wüchner, R., Larese, A., 2021. Nonconforming Dirichlet boundary conditions in implicit material point method by means of penalty augmentation. Acta Geotechnica doi:`https://doi.org/10.1007/s11440-020-01123-3`.

Coulomb, C.A., 1776. Essai sur une application des regles des maximis et minimis a quelques problemes de statique relatifs a l'architecture. Memoires de l'Academie Royale pres Divers Savants 7.

Crook, A.K., Yu, J., Wilson, S., Owen, D.R.J., 2006. Predictive modelling of structure evolution in sandbox experiments. Journal of Structural Geology 28, 729–744.

Cutillo, P.A., Screaton, E.J., Ge, S., 2003. Three-dimensional numerical simulation of fluid flow and heat transport within the Barbados Ridge accretionary complex. Journal of Geophysical Research 108, 2555.

Dahlen, F.A., 1984. Noncohesive critical Coulomb wedges: An exact solution. Journal of Geophysical Research 89, 10125–10133.

Davis, D., Suppe, J., Dahlen, F.A., 1983. Mechanics of fold-and-thrust belts and accretionary wedges. Journal of Geophysical Research 88, 1153–1172.

Egholm, D.L., Sandiford, M., Clausen, O.R., Nielsen, S.B., 2007. A new strategy for discrete element numerical models: 2. Sandbox applications. Journal of Geophysical Research 112, B05204.

Elliott, J., Jolivet, R., González, P., Avouac, J.P., Hollingsworth, J., Searle, M., Stevens, V., 2016. Himalayan megathrust geometry and relation to topography revealed by the Gorkha earthquake. Nature Geoscience 9, 174–180.

Fávero Neto, A.H., 2020. A Continuum Lagrangian Finite Deformation Computational Framework for Modeling Granular Flows. Ph.D. thesis. Stanford University.

Fávero Neto, A.H., Askarinejad, A., SM, S.M.S., Borja, R.I., 2020. Simulation of debris flow on an instrumented test slope using an updated Lagrangian particle method. Acta Geotechnica 15, 2757–2777.

Fávero Neto, A.H., Borja, R.I., 2018. Continuum hydrodynamics of dry granular flows employing multiplicative elastoplasticity. Acta Geotechnica 13, 1027–1040.

Feng, Y., Gray, K.E., 2019. XFEM-based cohesive zone approach for modeling near wellbore hydralic fracture complexity. Acta Geotechnica 14, 377–402.

Fullsack, P., 1995. An arbitrary Lagrangian-Eulerian formulation for creeping flows and its application in tectonic models. Geophsyical Journal International 120.

Gardner, M., Sitar, N., 2019. Coupled three-dimensional discrete element-lattice Boltzmann methods for fluid-solid interaction with polyhedral particles. International Journal for Numerical and Analytical Methods in Geomechanics 43, 2270–2287.

Gerya, T.V., Yuen, D.A., 2007. Robust characteristics method for modelling multiphase visco-elasto-plastic thermo-mechanical problems. Physics of the Earth and Planetary Interiors 163, 83–105.

Gingold, R., Monaghan, J., 1977. Smoothed particle hydrodynamics: theory and application to nonspherical stars. Monthly Notices of the Royal Astronomical Society 181, 375–389.

Graveleau, F., Malavieille, J., Dominguez, S., 2012. Experimental modelling of orogenic wedges: A review. Tectonophysics 538-540, 1–66.

Gray, G.G., Morgan, J.K., Sanz, P.F., 2014. Overview of continuum and particle dynamics methods for mechanical modeling of contractional geologic structures. Journal of Structural Geology 59, 19–36.

Herbert, J.W., Cooke, M.L., Souloumiac, P., Madden, E.H., Mary, B.C., Maillot, B., 2015. The work of fault growth in laboratory sandbox experiments. Earth and Planetary Science Letters 432, 95–102.

Hu, Y., Randolph, M., 1998. A practical numerical approach for large deformation problems in soil. International Journal for Numerical and Analytical Methods in Geomechanics 22, 327–350.

Itasca, 1999. PFC2D User's Guide Version 3.0. Itasca Consulting Group, Inc.

Jaeger, J., Cook, N., 1979. Rock Mechanics. Chapman and Hall.

Jameei, A.A., Pietruszczak, S., 2020. Embedded discontinuity approach for coupled hydromechanical analysis of fractured porous media. International Journal for Numerical and Analytical Methods in Geomechanics 44, 1880–1902.

Jiang, M., Zhang, A., Shen, Z., 2020. Granular soils: from DEM simulation to constitutive modeling. Acta Geotechnica 15, 1723–1744.

Jin, Y.F., Yuan, W.H., Yin, Z.Y., Cheng, Y.M., 2020. An edge-based strain smoothing particle finite element method for large deformation problems in geotechnical engineering. International Journal for Numerical and Analytical Methods in Geomechanics 44, 923–941.

Kaus, B.J.P., 2010. Factors that control the angle of shear bands in geodynamic numerical models of brittle deformation. Tectonophysics , 36–47.

Koons, P., 1990. Two-sided orogen: Collision and erosion from the sandbox to the Southern Alps, New Zealand. Geology 18, 679–682.

Kularathna, S., Liang, W., Zhao, T., Chandra, B., Zhao, J., Soga, K., 2021. A semi-implicit material point method based on frictional-step method for saturated soil. International Journal for Numerical and Analytical Methods in Geomechanics doi:`https://doi.org/10.1002/nag.3207`.

Lade, P.V., Kim, M.K., 1988. Single hardening constitutive model for frictional materials: II. Yield criterion and plastic work contours. Computers and Geotechnics 6, 13–29.

Liu, C., Prévost, J.H., Sukumar, N., 2019. Modeling branched and intersecting faults in reservoir-geomechanics models with the extended finite element method. International Journal for Numerical and Analytical Methods in Geomechanics 43, 2075–2089.

Liu, F., 2020. Modeling hydraulic fracture propagation in permeable media with an embedded strong discontinuity approach. International Journal for Numerical and Analytical Methods in Geomechanics 44, 1634–1655.

Liu, F., Borja, R.I., 2008. A contact algorithm for frictional crack propagation with the extended finite element method. International Journal for Numerical and Analytical Methods in Geomechanics 76, 1489–1512.

Liu, F., Borja, R.I., 2013. Extended finite element framework for fault rupture dynamics including bulk plasticity. International Journal for Numerical and Analytical Methods in Geomechanics 37, 3087–3111.

Liu, G.R., Liu, M.B., 2003. Smoothed Particle Hydrodynamics: A meshfree particle method. World Scientific.

Longo, A., Pastor, M., Sanavia, L., Manzanal, D., Stickle, M.M., Lin, C., Yague, A., Tayyebi, S.M., 2019. A depth average SPH model including $\mu(I)$ rheology and crushing for rock avalanches. International Journal for Numerical and Analytical Methods in Geomechanics 43, 833–857.

Lucy, L.B., 1977. A numerical approach to the testing of the fission hypothesis. The Astronomical Journal 82.

Ma, G., Regueiro, R., Zhou, W., Liu, J., 2019. Spatiotemporal analysis of strain localization in dense granular materials. Acta Geotechnica 14, 973–990.

Massoli, D., Koyi, H.A., Barchi, M.R., 2006. Structural evolution of a fold and thrust belt generated by multiple décollements analogue models and natural examples from the Northern Apennines (Italy). Journal of Structural Geology 28, 185–199.

Morgan, J.K., 2015. Effects of cohesion on the structural and mechanical evolution of fold and thrust belts and contractional wedges: Discrete element simulations. Journal of Geophysical Research: Solid Earth 120, 3870–3896.

Morgan, J.K., Boettcher, M.S., 1999. Numerical simulations of granular shear zones using the distinct element method 1. Shear zone kinematics and the micromechanics of localization. Journal of Geophysical Research 104, 2703–2719.

Mourgues, R., Lacoste, A., Garibaldi, C., 2014. The Coulomb critical taper theory applied to gravitational instabilities. Journal of Geophysical Research: Solid Earth 119, 754–765.

Naylor, M., Sinclair, H., 2005. A discrete element model for orogenesis and accretionary wedge growth. Journal of Geophysical Research 110, B12403.

Nguyen, N.H.T., Bui, H.H., Nguyen, G.D., 2020. An approach to calculating large strain accumulation for discrete element simulations of granular media. International Journal for Numerical and Analytical Methods in Geomechanics 44, 1525–1547.

Nikooei, M., Manzari, M.T., 2021. Investigating the effect of mixing layer rheology on granular flow over entrainable beds using SPH method. Computers and Geosciences 155, 104792.

Nilfouroushan, F., Pysklywec, R., Cruden, A., 2012. Sensitivity analysis of numerical scaled models of fold-and-thrust belts to granular material cohesion variation and comparison with analog equperiments. Tectonophysics 526-529, 196–205.

Niño, F., Philip, H., Chéry, J., 1998. The role of bed-parallel slip in the formation of blind thrust faults. Journal of Structural Geology 20, 503–516.

Nollet, S., Vennekate, G.J.K., Giese, S., Vrolijk, P., Urai, J.L., Ziegler, M., 2012. Localization patterns in sandbox-scale numerical experiments above a normal fault in basement. Journal of Structural Geology 39, 199–209.

Panian, J., Wiltschko, D., 2007. Ramp initiation and spacing in a homogenous thrust wedge. Journal of Geophysical Research 112, B05417.

Peng, C., Wang, S., Wu, W., Yu, H., Wang, C., Chen, J.Y., 2019. LOQUAT: an open-source GPU-accelerated SPH solver for geotechnical modeling. Acta Geotechnica 14, 1269–1287.

Persson, K.S., 2001. Effective indenters and the development of doubly vergent orogens: Insights from analogue sand models, in: Koyi, H.A., Mancktelow, N.S. (Eds.), Tectonic Modeling. Geological Society of America. volume 193, pp. 191–206.

Pollard, D.D., Fletcher, R.C., 2005. Fundamentals of Structural Geology. Cambridge University Press.

Ramachandran, P., Bhosale, A., Puri, K., Negi, P., Muta, A., Dinesh, A., Menon, D., Govind, R., Sanka, S., Sebastian, A.S., Sen, A., Kaushik, R., Kumar, A., Kurapati, V., Patil, M., Tavker, D., Pandey, P., Kaushik, C., Dutt, A., Agarwal, A., 2020. PySPH: a Python-based framework for smoothed particle hydrodynamics. `arXiv:1909.04504`.

Reber, J.E., Cooke, M.L., Dooley, T.P., 2020. What model material to use? A Review on rock analogs for structural geology and tectonics. Earth-Science Reviews 202, 103107.

Rockfield, 2017. Eflen explicit manual. (version 4.10) ed. Rockfield Software. Swansea, UK.

Roscoe, K.H., 1970. The influence of strains in soil mechanics. Géotechnique 20, 129–170.

Roscoe, K.H., Burland, J.H., 1968. On the generalized stress-strain behavior of 'wet' clay, in: Heyman, J., Leckie, F.A. (Eds.), Engineering Plasticity, Cambridge University Press. pp. 535–609.

Rowe, K.T., Screaton, E.J., Ge, S., 2012. Coupled fluid flow and deformation modeling of the frontal thrust region of the Kumano Basin transect, Japan: Implications for fluid presures and decollement downstepping. Geochemistry Geophysics Geosystems 13, Q0AD23.

Ruh, J.B., Kaus, B.J.P., Burg, J.P., 2012. Numerical investigation of deformation mechanics in fold-and-thrust belts: Influence of rheology of single and multiple décollement. Tectonics 31, TC3005.

Saffer, D.M., Bekins, B.A., 2002. Hydrologic controls on the morphology and mechanics of accretionary wedges. Geology 30, 271–274.

Saffer, D.M., Bekins, B.A., 2006. An evaluation of factors influencing pore pressure in accretionary complexes: Implications for taper angle and wedge mechanics. Journal of Geophysical Research 111, B04101.

Sanz, P.F., Borja, R.I., Pollard, D.D., 2007. Mechanical aspects of thrust faulting driven by far-field compression and their implications for fold geometry. Acta Geotechnica 2, 17–31.

Sanz, P.F., Pollard, D.D., McCory, P.A., Borja, R.I., 2008. Mechanical models of fracture activation and slip on bedding surfaces during folding of the asymmetric anticline at sheep mountain, wyoming. Journal of Structural Geology 30, 1177–1191.

Schreurs, G., Buiter, S., Boutelier, J., Burberry, C., Callot, J.P., Cavozzi, C., Cerca, M., Chen, J.H., Cristallini, E., Cruden, A., Cruz, L., Daniel, J.M., Poian, G.D., Garcia, V., Gomes, V., Grall, C., Guillot, Y., Guzmán, C., Hidayah, T.N., Hilley, G., Klinkmüller, M., Koyi, H., Lu, C.Y., Maillot, B., Meriaux, C., Nilfouroushan, F., Pan, C.C., Pillot, D., Portillo, R., Rosenau, M., Schellart, W., Schlische, R., Take, A., Vendeville, B., Vergnaud, M., Vettori, M., Wang, S.H., Withjack, M., Yagupsky, D., Yamada, Y., 2016. Benchmarking analogue models of brittle thrust wedges. Journal of Structural Geology 92, 116–139.

Schreurs, G., Buiter, S.J., Boutelier, D., Corti, G., Costa, E., Cruden, A.R., Daniel, J.M., Hoth, S., Koyi, H., Kukowski, N., Lohrmann, J., Ravaglia, A., Schlische, R.W., Withjack, M.O., Yamada, Y., Cavozzi, C., Del Ventisette, C., Brady, J.A.E., Hoffman-Rothe, A., Mengus, J.M., Montanari, D., Nilfouroushan, F., 2006. Analogue benchmarks of shortening and extension experiments. Geological Society, London Special Publications 253, 1–27.

Schwaiger, H.F., 2007. An Implementation of Smoothed Particle Hydrodynamics for Large Deformation, History Dependent Geomaterials With Applications to Tectonic Deformation. Ph.D. thesis. University of Washington.

Scovazzi, G., Colomés, O., Abboud, N., Veveakis, M., del Castillo, E.M., Valiveti, D., Huang, H., 2021. A blended transient/quasistatic Lagrangian framework for salt tectonics simulations with stabilized tetrahedral finite elements. International Journal for Numerical Methods in Engineering 122, 3489–3524.

Semnani, S.J., White, J.A., Borja, R.I., 2016. Thermoplasticity and strain localization in transversely isotropic materials based on anisotropic critical state plasticity. International Journal for Numerical and Analytical Methods in Geomechanics 40, 2423–2449.

Sheikh, B., Qiu, T., Ahmadipur, A., 2020. Comparison of SPH boundary approaches in simulating frictional soil-structure interaction. Acta Geotechnica doi:`https://doi.org/10.1007/s11440-020-01063-y`.

Shen, Z., Hao, F., Wang, Z., Jiang, M., 2019. Evolution of mesoscale bounded particle clusters in cemented granular material. Acta Geotechnica 14.

Shiozawa, S., Lee, S., Wheeler, M.F., 2019. The effect of stress boundary conditions on fluid-driven fracture propagation in porous media using a phase-field modeling approach. International Journal for Numerical and Analytical Methods in Geomechanics 43, 1316–1340.

Simo, J.C., Oliver, J., Armero, F., 1993. An analysis of strong discontinuities induced by strain-softening in rate-independent inelastic solids. Computational Mechanics 12, 277–296.

Simpson, G., 2006. Modelling interactions between fold-thrust belt deformation, foreland flexure and surface mass transport. Basin Research , 125–143.

Simpson, G., 2011. Mechanics of non-critical fold-thrust belts based on finite element models. Tectonophysics 499, 142–155.

Song, X., Borja, R.I., 2014a. Finite deformation and fluid flow in unsaturated soils with random heterogeneity. Vadose Zone Journal 13.

Song, X., Borja, R.I., 2014b. Mathematical framework for unsaturated flow in the finite deformation range. International Journal for Numerical Methods in Engineering 14, 658–682.

Song, X., Menon, S., 2019. Modeling of chemo-hydromechanical behavior of unsaturated porous media: a nonlocal approach based on integral equations. Acta Geotechnica 14, 727–747.

Soto, R., Storti, F., Casas-Sainz, A.M., 2006. Impact of backstop thickness lateral variations on the tectonic architecture of orogens: Insights from sandbox analogue modeling and application to the pyrenees. Tectonics 25, TC2005.

Stockmal, G.S., Beaumont, C., Nguyen, M., Lee, B., 2007. Whence the Mountains? Inquiries into the Evolution of Orogenic Systems: A Volume in Honor of Raymond A. Price. The Geological Society of America. chapter Mechanics of thin-skinned fold-and-thrust belts: Insights from numerical models. 433, pp. 63–98.

Storti, F., Salvini, F., 2000. Synchronous and velocity-partioned thrusting and thrust polarity reversal in experimentally produced, doubly-vergent thrust wedges: Implications for natural orogens. Tectonics 19, 378–396.

Su, Y.C., Sewell, T., Chen, Z., 2021. Comparative investigation of shear-band evolution using discrete and continuum-based particle methods. Acta Geotechnica doi:`https://doi.org/10.1007/s11440-021-01150-8`.

Sun, W., Fish, J., 2021. Coupling of non-ordinary state-based peridynamics and finite element method for fracture propagation in saturated porous media. International Journal for Numerical and Analytical Methods in Geomechanics 45, 1260–1281.

Tran, H.T., Wang, Y., Nguyen, G.D., Kodikara, J., Sanchez, M., Bui, H.H., 2019. Modelling 3D desiccation cracking in clayey soils using a size-dependent SPH computational approach. Computers and Geotechnics 116, 103209.

Vignjevic, R., Djordjevic, N., Gemkow, S., De Vuyst, T., Campbell, J., 2014. SPH as a nonlocal regularisation method: Solution for instabilities due to strain-softening. Computer Methods in Applied Mechanics and Engineering 277, 281–304.

Violeau, D., 2012. Fluid Mechanics and the SPH Method. Oxford University Press.

Wang, L., Zhang, X., Tinti, S., 2021. Large deformation dynamic analysis of progressive failure in layered clayey slopes under seismic loading using the particle finite element method. Acta Geotechnica doi:`https://doi.org/10.1007/s11440-021-01142-8`.

Wang, W.H., Davis, D.M., 1996. Sandbox model simulation of forearc evolution and noncritical wedges. Journal of Geophysical Research: Solid Earth 101, 11329–11339.

Wang, Y., Bui, H.H., Nguyen, G.D., Ranjith, P.G., 2019. A new SPH-based continuum framework with an embedded fracture process zone for modelling rock fracture. International Journal of Solids and Structures 159, 40–57.

Wang, Y., Tran, H.T., Nguyen, G.D., Ranjith, P.G., Bui, H.H., 2020. Simulation of mixed-mode fracture using SPH particles with an embedded fracture process zone. International Journal for Numerical and Analytical Methods in Geomechanics 44, 1417–1445.

Willett, S., Beaumont, C., Fullsack, P., 1993. Mechanical model for the tectonics of doubly vergent compressional orogens. Geology 21, 371–374.

Willett, S.D., 1999. Rheological dependence of extension in wedge models of convergent orogens. Tectonophysics 305, 419–435.

Wolf, H., Konig, D., Triantafylldis, T., 2003. Experimental investigation of shear band patterns in granular material. Journal of Structural Geology 25, 1129–1240.

Wu, Q.X., Xu, T.T., Yang, Z.X., 2020. Diffuse instability of granular material under various drainage conditions: discrete element simulation and constitutive modeling. Acta Geotechnica 15, 1763–1778.

Xu, G., Gutierrez, M., He, C., Meng, W., 2020a. Discrete element modeling of transversely isotropic rocks with non-continuous planar fabrics under Brazilian test. Acta Geotechnica 15, 2277–2304.

Xu, W.J., Liu, G.Y., Yang, H., 2020b. Study on the mechanical behavior of sands using 3D discrete element method with realistic particle models. Acta Geotechnica 15, 2813–2828.

Yan, B., Regueiro, R.A., 2019. Three-dimensional discrete element method parallel computation of Cauchy stress distribution over granular materials. International Journal for Numerical and Analytical Methods in Geomechanics 43, 974–1004.

Yang, J., Tchelepi, H.A., Kovscek, A.R., 2021. Phase-field modeling of rate-dependent fluid-driven fracture initiation and propagation. International Journal for Numerical and Analytical Methods in Geomechanics 45, 1029–1048.

Yin, Q., Liu, Y., Borja, R.I., 2021. Mechanisms of creep in shale from nanoscale to specimen scale. Computers and Geotechnics 136, 104138.

Yuan, W.H., Wang, H.C., Zhang, W., Dai, B.B., Liu, K., Wang, Y., 2021. Particle finite element method implementation for large deformation analysis using Abaqus. Acta Geotechnica doi:`https://doi.org/10.1007/s11440-020-01124-2`.

Zhan, L., Peng, C., Zhang, B., Wu, W., 2020. A SPH framework for dynamic interaction between soil and rigid body system with hybrid contact method. International Journal for Numerical and Analytical Methods in Geomechanics 44, 1446–1471.

Zhang, Q., Borja, R.I., 2021. Poroelastic coefficients for anisotropic single and double porosity media. Acta Geotechnica doi:`https://doi.org/10.1007/s11440-021-01184-y`.

Zhao, T., Liu, Y., 2020. A novel random discrete element analysis of rock fragmentation. International Journal for Numerical and Analytical Methods in Geomechanics 44, 1386–1395.

Zhao, Y., Borja, R.I., 2020. A continuum framework for coupled solid deformation–fluid flow through anisotropic elastoplastic porous media. Computer Methods in Applied Mechanics and Engineering 369, 113225.

Zhao, Y., Borja, R.I., 2021. Anisotropic elastoplastic response of double-porosity media. Computer Methods in Applied Mechanics and Engineering 380, 113797.

Zhao, Y., Semnani, S.J., Yin, Q., Borja, R.I., 2018. On the strength of transversely isotropic rocks. International Journal for Numerical and Analytical Methods in Geomechanics 42, 1917–1934.

Zhou, S., Zhuang, X., 2020. Phase field modeling of hydraulic fracture propagation in transversely isotropic poroelastic media. Acta Geotechnica 15, 2599–2618.

Zhou, S.W., Xia, C.C., 2019. Propagation and coalescence of quasi-static cracks in Brazilian disks: an insight from a phase field model. Acta Geotechnica 14, 1195–1214.

Zubeldia, E.H., Fourtakas, G., Rogers, B.D., Farias, M.M., 2018. Multi-phase SPH model for simulation of erosion and scouring by means of the shields and Drucker-Prager criteria. Advances in Water Resources 117, 98–114.